

1 **Seismic structure of the St. Paul Fracture Zone and Late Cretaceous to Mid**  
 2 **Eocene oceanic crust in the equatorial Atlantic Ocean near 18°W**

3

4 Kevin Growe<sup>1,2</sup>, Ingo Grevemeyer<sup>1</sup>, Satish C. Singh<sup>2</sup>, Milena Marjanović<sup>2</sup>, Emma P. M. Gregory<sup>2</sup>, Cord Papenberg<sup>1</sup>,  
 5 Venkata Vaddineni<sup>2</sup>, Laura Gómez de la Peña<sup>1</sup>, and Zhikai Wang<sup>2</sup>

6

7 <sup>1</sup>GEOMAR Helmholtz Centre for Ocean Research Kiel

8 <sup>2</sup>Université de Paris, Institut de Physique du Globe de Paris; CNRS, Paris, France

9

10 Corresponding author: Kevin Growe (kevin.growe93@web.de)

11 **Key Points:**

- 12 • Seismic structure along the St. Paul fracture zone reflects magmatically accreted oceanic  
 13 crust
- 14 • Oceanic crust across St. Paul shows only small thickness variations, lacking evidence for  
 15 regional crustal thinning near fracture zones
- 16 • Magmatic nature of crust supports a mechanism where transform crust is augmented  
 17 before being turned into a fracture zone

## 18 **Abstract**

19 Plate tectonics characterize transform faults as conservative plate boundaries where the  
20 lithosphere is neither created nor destroyed. In the Atlantic, both transform faults and their  
21 inactive traces, fracture zones, are interpreted to be structurally heterogeneous, representing thin,  
22 intensely fractured, and hydrothermally altered basaltic crust overlying serpentinized mantle.  
23 This view, however, has recently been challenged. Instead, transform zone crust might be  
24 magmatically augmented at ridge-transform intersections before becoming a fracture zone. Here,  
25 we present constraints on the structure of oceanic crust from seismic refraction and wide-angle  
26 data obtained along and across the St. Paul fracture zone near 18°W in the equatorial Atlantic  
27 Ocean. Most notably, both crust along the fracture zone and away from it shows an almost  
28 uniform thickness of 5-6 km, closely resembling normal oceanic crust. Further, a well-defined  
29 upper mantle refraction branch supports a normal mantle velocity of 8 km/s along the fracture  
30 zone valley. Therefore, the St. Paul fracture zone reflects magmatically accreted crust instead of  
31 the anomalous hydrated lithosphere. Little variation in crustal thickness and velocity structure  
32 along a 200 km long section across the fracture zone suggests that distance to a transform fault  
33 had negligible impact on crustal accretion. Alternatively, it could also indicate that a second  
34 phase of magmatic accretion at the proximal ridge-transform intersection overprinted features of  
35 starved magma supply occurring along transform faults.

36

## 37 **Plain Language Summary**

38 Transform faults are tectonic plate boundaries where the lithosphere is neither created nor  
39 destroyed. Previous studies have revealed that many Atlantic transform faults and their inactive  
40 traces, fracture zones, are characterized by a strongly altered and fractured crust that is reduced  
41 in thickness and is overlying altered mantle rocks. Conversely, recent results propose a  
42 mechanism of secondary magma supply at the ridge-transform intersections, that enhances the  
43 crust while being transferred from the transform fault to the fracture zone domain. Here, we  
44 present results from seismic experiments along and across the St. Paul fracture zone near 18°W  
45 in the equatorial Atlantic Ocean. We observe a nearly uniform crustal thickness of 5-6 km and  
46 waves traveling through the upper mantle with a velocity of 8 km/s. Both observations indicate a  
47 magmatic formation of the crust and the absence of strong alteration of the upper mantle. The  
48 relatively constant crustal thickness and little variation in seismic velocities along the 200 km  
49 long profile across the fracture zone suggests that the distance to the transform fault had no  
50 significant impact on the crustal formation process. Alternatively, secondary magma supply at  
51 the ridge-transform intersection enhancing the crust could overprint effects from any anomalous  
52 formation conditions.

53

## 54 **1 Introduction**

55 Plate tectonics separates Earth's surface into rigid plates (McKenzie, 1967; Morgan,  
56 1968), and deformation or relative motion between plates reveals three different types of oceanic  
57 plate boundaries: (i) constructive plate boundaries at mid-ocean ridges (MOR) where new  
58 seafloor is created, (ii) destructive plate boundaries at subduction zones where the oceanic  
59 lithosphere is transferred into the mantle and recycled, and (iii) conservative plate boundaries

60 and hence transform faults (TF) where the lithosphere is neither created nor destroyed as plates  
61 move past each other (Morgan, 1968). In ocean basins, transform faults offset MOR by tens to  
62 several hundreds of kilometers (Searle et al., 1994), splitting them into first-order spreading  
63 segments (Macdonald et al., 1988). They are long-lived features, and in the equatorial Atlantic,  
64 the largest transform faults, namely Chain, Romanche, and St. Paul, can be followed along their  
65 inactive traces, called fracture zones (FZ), towards the margins of the Atlantic Ocean (Wilson,  
66 1965). Fracture zones are prominent linear features on the ocean floor that were identified and  
67 named before plate tectonics linked them to seafloor spreading (Menard, 1955; 1967).

68 Oceanic crust formed along a spreading ridge is generally believed to remain largely  
69 unchanged as it is moved by plate motion away from the active plate boundary. Its structure can  
70 be best described with respect to a layered structure, where the crust is divided into two main  
71 distinct lithologic layers exhibiting different seismic properties (e.g., Raitt, 1963). The upper  
72 crust (layer 2) consists of pillow basalts overlaying a basaltic sheeted dike complex (e.g., Vine &  
73 Moores, 1972) and reveals high velocity gradients of 1-2 s<sup>-1</sup> and velocities from 3-5 km/s just  
74 below the basement to 6.3-6.8 km/s at a depth of 1-2 km below the basement (e.g., Grevemeyer  
75 et al., 2018; White et al. 1992; Whitmarsh, 1978). The mid- and lower crust (layer 3) instead  
76 consist of plutonic, mostly gabbroic, rocks and has low velocity gradients of 0.1-0.2 s<sup>-1</sup> and  
77 velocities from ~6.6 km/s at the top of the layer to 7.2 km/s at its base (e.g., Carlson & Miller,  
78 2004; Vine & Moores, 1972). The thickness of layer 3 is much more variable than the thickness  
79 of layer 2 such that variations in crustal thickness in several studies are related to thickness  
80 variations of layer 3 (e.g., Mutter & Mutter, 1993).

81 It has long been recognized that oceanic crust varies along spreading segments, with the  
82 thickest crust formed at a segment center away from major ridge crest discontinuities and the  
83 thinnest crust at segment ends or transform faults (e.g., Macdonald et al., 1988; Tolstoy et al.,  
84 1993). Along fast-spreading ridges, thickness variations are reasonably small, within some  
85 hundreds of meters to less than a kilometer (e.g., Canales et al., 2003). At slow- and ultraslow-  
86 spreading ridges, crust of ~7-9 km thickness may occur at segment centers and decrease to only  
87 4-6 km at segment ends (e.g., Canales et al., 2000; Dannowski et al., 2011; Grevemeyer et al.,  
88 2018; Niu et al., 2015). These along-axis thickness variations can be best explained by focused  
89 mantle upwelling at segment centers and lateral melt transport, suggesting that mantle upwelling  
90 is intrinsically plume-like (3-D) beneath a slow-spreading ridge but more sheet-like (2-D)  
91 beneath a fast-spreading ridge (Bell & Buck, 1992; Lin & Morgan, 1992).

92 Along-axis changes in oceanic crustal architecture suggest that the end of spreading  
93 segments and hence transform faults represent the magmatically starved end-member of the  
94 oceanic crust (e.g., Detrick et al., 1993; White et al., 1984) where tectonic stresses rotate by tens  
95 of degrees over a very short distance (Morgan & Parmentier, 1984), changing from normal  
96 faulting at the spreading axis to strike-slip along the transform (e.g., Sykes, 1967). In the Pacific,  
97 the crustal structure at transform faults reveals a drop of seismic P-wave velocity in the active  
98 strike-slip fault, indicating the presence of high porosities along the tectonically active fault trace  
99 (Roland et al., 2012). However, it shows little evidence for reduced melt supply as crustal  
100 thickness across the fast-slipping transforms indicates only a small reduction, which is in the  
101 order of some hundreds of meters (Roland et al., 2012). In contrast, some transform faults in the  
102 Atlantic exhibit thin crust ~4-5 km thick (e.g., Ambos & Hussong, 1986; Detrick et al., 1982;  
103 Whitmarsh & Calvert, 1986) along transform valleys which is 1-2 km thinner when compared to  
104 the neighboring normal oceanic crust (e.g., Grevemeyer et al., 2018; van Avendonk et al., 2017;

105 White et al., 1992). The above observations led to the conclusion that lithosphere along  
106 transform faults and fracture zones might be intensely fractured, faulted, and composed of  
107 hydrothermally altered basaltic and gabbroic rocks overlying ultramafics that might be  
108 extensively serpentinized (Detrick et al., 1993; White et al., 1984).

109 A recent study suggests that the crust beneath the Chain fracture zone in the equatorial  
110 Atlantic region has a nearly normal crustal thickness (Marjanović et al., 2020). This observation  
111 has been independently supported using global bathymetric observations and numerical  
112 simulation on transform fault tectonics (Grevemeyer et al., 2021) suggesting that crust is (i)  
113 initially magmatically emplaced near a ridge-transform intersection (RTI), (ii) experiences  
114 tectonic deformation, and extension while being moved along the transform fault and (iii) finally  
115 it is augmented by the second stage of magmatism as it passes the opposing RTI. If correct, the  
116 formation of crust at transform faults should occur in three distinctive phases, suggesting that the  
117 structure of crust present below the valley of an active transform fault should differ profoundly  
118 from crust found along its fracture zones.

119 Here, we use two state-of-the-art seismic profiles shot in 2017 and 2018 with modern  
120 seismic refraction and wide-angle equipment surveying the St. Paul fracture zone near 18°W in  
121 the equatorial Atlantic region (Fig. 1). The seismic data are well-suited for seismic tomography  
122 in order to study the structure along a 140 km-long roughly west-east running profile in the  
123 valley of the St. Paul fracture zone and along a 300 km-long north-south trending profile  
124 crossing the fracture zone and sampling the adjacent mature oceanic crust. The north-south  
125 striking profile runs parallel to the trend of the Mid-Atlantic Ridge (MAR) and hence should  
126 reveal features governed by changes in melt supply towards a transform fault and lateral melt  
127 transport, which is expected to diminish when approaching transform faults (e.g., Lin et al.,  
128 1990; Macdonald et al., 1988; White et al., 1984). The crustal and upper mantle velocity  
129 structures are derived from a joint tomographic inversion of first arrival travel times and wide-  
130 angle reflections from the crust-mantle boundary, providing high-resolution constraints on the  
131 seismic velocity structure and crustal thickness along the fracture zone and the dependence of  
132 crustal accretion as a function of distance to a fracture zone.

## 133 2 Regional Setting of the St. Paul Fracture Zone and Study Area

### 134 2.1 Regional Setting of the St. Paul Fracture Zone

135 The St. Paul fracture zone (SPFZ) is one of the major east-west striking equatorial fracture zones  
136 of the Atlantic Ocean. At the active MAR, the St. Paul, Romanche and Chain transform faults  
137 offset the ridge crest by ~1800 km, causing an age variation of 90 Myr over 400 km north-south  
138 distance (Müller et al., 2008). The active domain of the St. Paul transform fault system offsets  
139 the MAR by ~600 km and can be subdivided into four strike-slip faults; sandwiched in between  
140 are three short intra-transform spreading segments (Fig. 1a). Maia et al. (2016) studied the  
141 northern TF segment and found a complex tectonic regime revealing a transpressional zone  
142 exhuming deformed and serpentinized mantle rocks, triggered as a response to a change of  
143 relative plate motion ~11 Myr ago. The fossil trace of the transform fault, the fracture zone can  
144 be followed using the vertical gravity gradient (Sandwell et al., 2014) across the entire Atlantic  
145 Ocean, from the continental shore of Liberia in the east to the Amazonas Basin in the west,  
146 resulting in a total length of ~3000 km. For ages greater than 20 Myr (Mueller et al., 2008) away  
147 from both RTI, the bathymetry data indicate the presence of only two fracture zone valleys,  
148 suggesting that today's complex transform-fault-system developed roughly 20 Myr ago.

149 Using 2-D ultra-deep multichannel seismic reflection data, Mehouchi and Singh (2018) imaged  
150 the lithosphere-asthenosphere boundary along a north-south striking line and revealed a  
151 southward thinning of the lithosphere, mimicking the age contrast across the system of fracture  
152 zones at ~18°W.

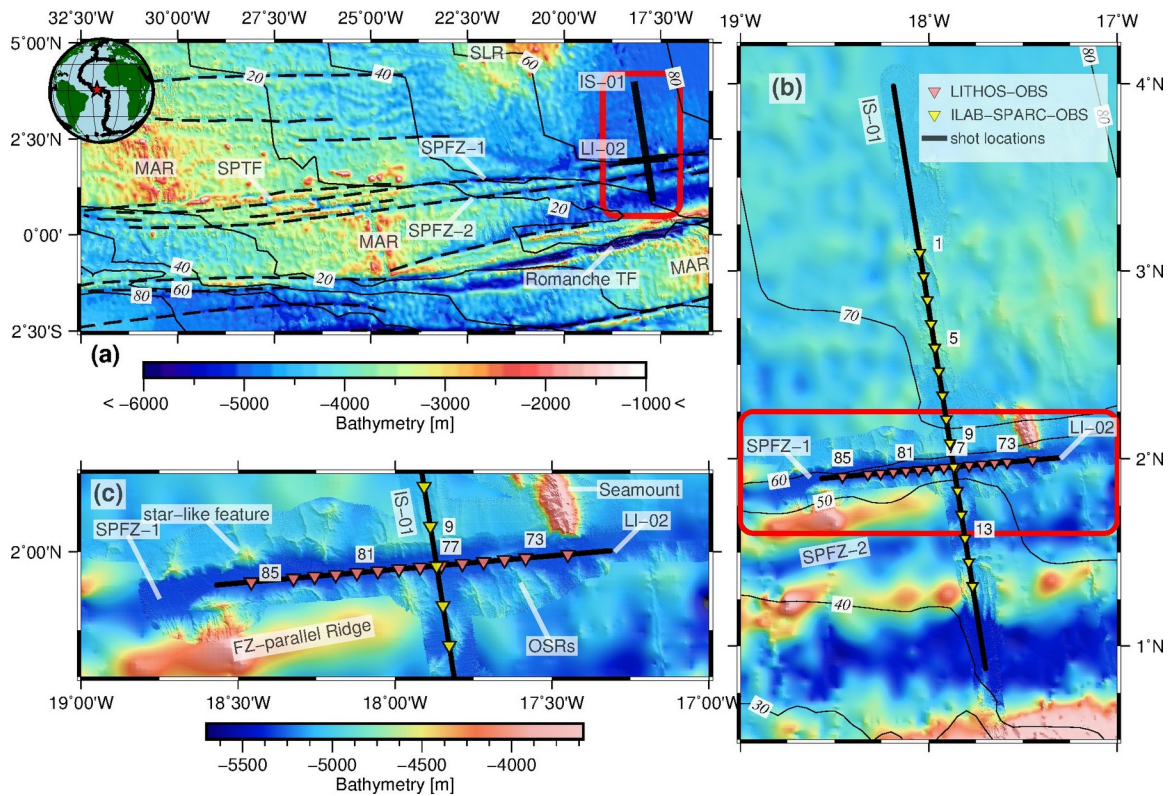
153

### 154 2.2 Study Area

155 Within our study area, ~680 km east from the active St. Paul transform fault system (Fig. 1a), the  
156 ~10 km wide northernmost St. Paul fracture zone valley (SPFZ-1) separates ~70 Ma oceanic  
157 lithosphere in the north from 40-50 Ma lithosphere in the south (Müller et al., 2008). Here, the  
158 valley is covered by sediments up to a kilometer thick, creating a smooth surface but still  
159 forming a 200-300 m deep valley with respect to the surrounding ocean floor (Fig. 1c). Its  
160 younger southern edge is flanked by significantly rougher bathymetry, revealing ridge-like  
161 features aligned mostly perpendicular to the FZ that we interpret as overshooting ridges, as  
162 observed near RTIs globally (e.g., Grevemeyer et al., 2021; Lonsdale, 1986; Marjanović et al.,  
163 2020). The older northern flank of the FZ can be subdivided into two distinct domains (Fig 1c).  
164 The north-western area to the west of the intersection of seismic profiles shows ridge- and dome-  
165 like features mostly parallel to the fracture zone. In contrast, the north-eastern domain reveals a  
166 rather smooth seafloor, except for a seamount-like structure located at the eastern limit of the  
167 west-east striking seismic line LI-02.

168 The north-south striking seismic line IS-01 ran over a smooth seafloor of an almost constant  
 169 depth to the north of St. Paul, except for two ridge-like features near OBS 1 and OBS 5 (Fig 1b).  
 170 The bathymetry to the south of SPFZ-1 is significantly rougher, showing east-west trending  
 171 ridge-like features separating SPFZ-1 from a second, parallel fracture zone valley in the south  
 172 (SPFZ-2) near OBS13. SPFZ-2 is related to the southernmost TF segment of the modern active  
 173 TF system of St. Paul (Fig. 1a). The seismic line is limited in the south by another FZ parallel  
 174 ridge south of SPFZ-2 and a deep basin just north of the Romanche TF (Fig. 1a, b).

175



177

178 **Figure 1:** Regional and survey map in the equatorial Atlantic Ocean. **(a)** Bathymetric map showing  
 179 survey location and tectonic setting around the SPFZ. The bathymetry is from TOPEX satellite gravity  
 180 data (Sandwell et al., 2014). Thin labelled black lines denote crustal age after Müller et al. (2008) with an  
 181 interval of 20 Myrs. Dashed lines denote fracture zones mapped by Matthews et al. (2011). Plate  
 182 boundaries on inset globe are from Bird (2003) and red star indicates the survey location. The thick black  
 183 lines represent the two survey lines (LI-02 and IS-01). Red box marks the survey area shown in (b). The  
 184 main regional tectonic features are labeled (see definition of acronyms at the end of the caption). **(b)**  
 185 Survey area showing shot and OBS locations for both seismic lines (note legend). Every fourth OBS is  
 186 labeled. The bathymetry is combined by TOPEX data and acquired shipboard high resolution multibeam  
 187 echo-sounder data (LITHOS: 100x100 m; ILAB-SPARC: 50x50 m). The crustal ages are indicated by  
 188 thin black contours and labelled with an interval of 10 Myrs. The red box depicts the closeup map shown  
 189 in (c). **(c)** Closeup of bathymetric map of the surveyed transect of the SPFZ-1 using the same color scale  
 190 as in (b). Prominent bathymetric features are labeled. Remaining features are displayed as in (b).  
 191 Acronyms: MAR - Mid-Atlantic Ridge, TF - Transform Fault, SPTF - St.Paul Transform Fault, SPFZ -  
 192 St.Paul Fracture Zone, SLR - Sierra Leone Rise, OSRs - Overshooting Ridges.

193

### 194 **3 Data Acquisition and Processing**

195 In the framework of the Trans-Atlantic-iLAB and LITHOS projects, several OBS based seismic  
 196 refraction lines, as well as multichannel seismic reflection lines, were acquired during three  
 197 cruises in the central equatorial Atlantic Ocean from 2015-2018. In this study, we present the  
 198 results from the two seismic refraction and wide-angle profiles along and across the St. Paul  
 199 fracture zone, at 2°N/18° W, hereafter named as profiles LI-02 and IS-01 (see Supplementary  
 200 Figs S1 and S2). Profile IS-01 is coincident with the seismic reflection profile of Mehouchi and  
 201 Singh (2018).

#### 202 **3.1 Acquisition LI-02**

203 Profile LI-02 was acquired during the LITHOS cruise onboard the German R/V Maria S. Merian  
 204 in December 2017, where 12 four-component ocean bottom seismometers (OBS) and two one-  
 205 component ocean bottom hydrophones (OBH) with a spacing of 7.5 - 15 km were deployed  
 206 within the fracture zone valley (Fig. 1c). For simplicity, we will refer to all receiver types as  
 207 OBS. A total of 875 shots were fired at 210 bars on a 142 km long east-west orientated transect.  
 208 A shot time interval of 90 s with a vessel speed of ~3.5 knots led to an average spatial shot  
 209 interval of ~160 m. The two airgun sub-arrays each consisted of six G-guns, provided a total  
 210 volume of 86 l, and were towed at a depth of 7.5 m. The OBS data were sampled at 250 Hz. All  
 211 instruments recorded good quality data containing crustal (Pg) and mantle (Pn) refraction arrivals  
 212 up to offsets of 90 km, and all but two OBS, OBS 82 and 85, also recorded wide-angle  
 213 reflections from the Moho (PmP) (Fig. 2). Pg and PmP arrivals could be picked mostly between  
 214 5-25 and 15-30 km offsets, respectively. Pn arrivals could be picked mostly up 60 km offset and  
 215 even up to 80-90 km for some record sections (see all record sections in Figures S1a-n in the  
 216 supplementary material). Since no streamer data were acquired along the profile, the basement  
 217 depth and the sediment structures were obtained by mirror imaging (Supplementary material Fig.  
 218 S3) of the hydrophone component of OBS receiver gathers (e.g., Grion et al., 2007).

## 219 3.2 Acquisition IS-01

220 Line IS-01 is the northernmost part of the north-south profile acquired during the ILAB-SPARC  
221 cruise aboard the French R/V *Pourquoi Pas?* in 2018. The profile is in total 850 km-long,  
222 crossing farther south the Romanche transform fault ( $\sim 0^\circ\text{N}$ ) (Gregory et al., 2021) and the Chain  
223 fracture zone ( $\sim 2^\circ\text{S}$ ) (Marjanović et al., 2020). Here, we use the data from the northernmost 350  
224 km of the line containing 15 four-component OBS with an average instrument spacing of 14.2  
225 km. The OBS data were sampled at 250 Hz. Most OBS receiver gathers provide good quality  
226 data where both refraction and wide-angle reflection arrivals can be identified with confidence  
227 (Fig. 2). Pg and PmP arrivals were picked mostly between 5-25 and 15-35 km offset,  
228 respectively. Pn arrivals could be picked mostly up 50 km offset (Fig. S2). A summary of the  
229 acquisition parameters for the two refraction profiles is provided in Table S1.

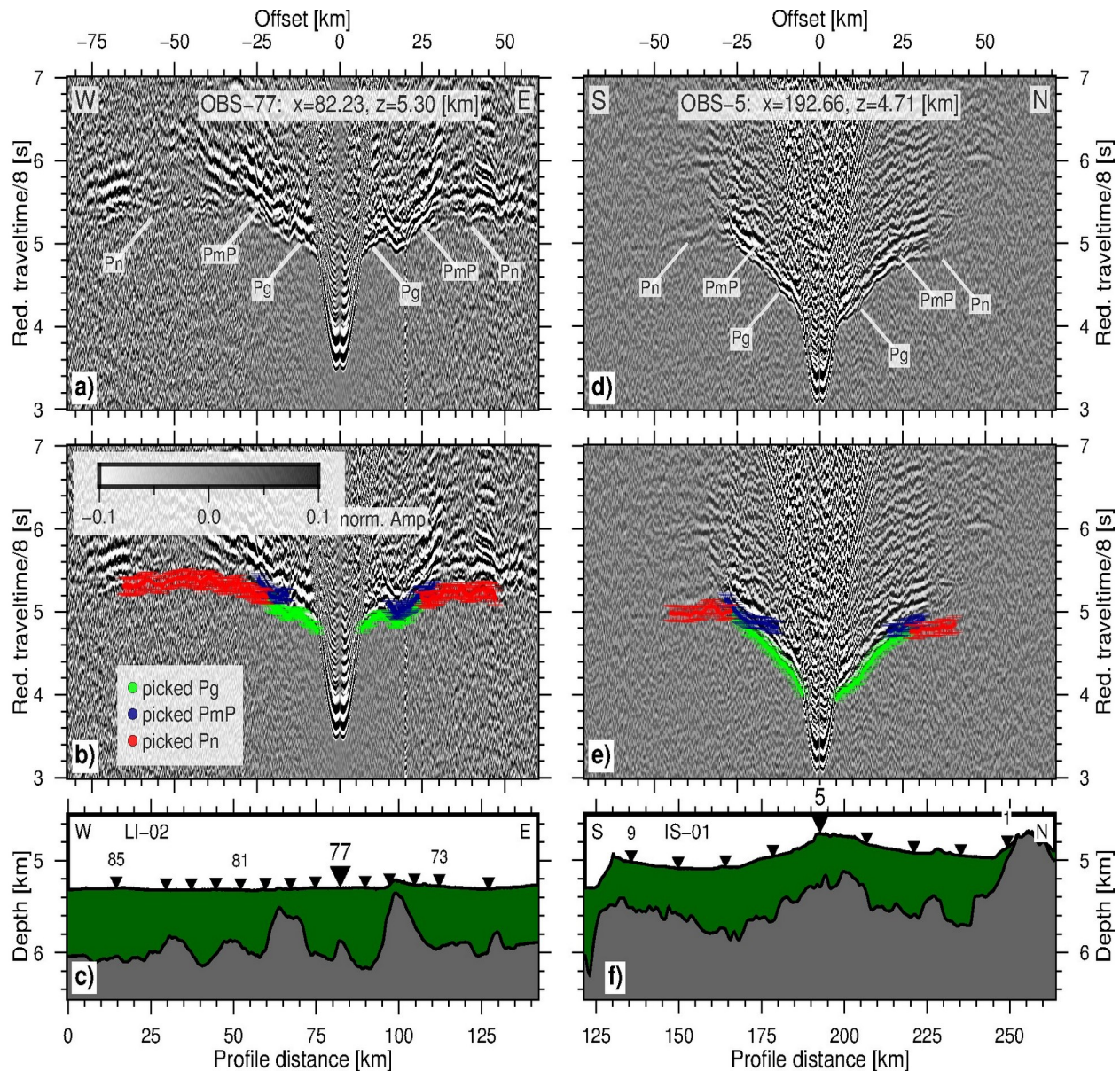
230 A total of 1168 shots were fired at a pressure of 140 bars and at a source interval of 300 m. The  
231 larger shot interval was chosen to minimize the noise level in the water column for later arrivals.  
232 Two sub-arrays containing eight G-guns each provided a total volume of 82 liters and were  
233 towed at a depth of 10 m. Real-time source monitoring provided excellent conditions for a well-  
234 tuned signal which is critical for such an experiment.

235 Simultaneously, a 6 km-long streamer containing 960 hydrophones, grouped with a spacing of  
236 6.25 m, was towed at a depth of 12 m to acquire multi-channel seismic (MCS) data along the  
237 line. A basic processing sequence included bandpass filtering from 5-125 Hz, normal-move out  
238 (NMO) based stacking, and migration with a constant velocity of 1.5 km/s, which provided  
239 seismic images of the sediment cover and the depth of the igneous basement (Supplementary  
240 material Fig. S4). Due to the large shot interval and consequently low fold, the quality of the  
241 seismic image is poor below the basement. The MCS data were therefore mainly used to  
242 constrain the depth and shape of the basement below the sediment cover. Thus, both seafloor and  
243 basement were picked on the post-stack time-migrated section and converted to depth for the  
244 tomographic travel time inversion using the acoustic velocity of water and a constant velocity for  
245 sediments of 1.86 km/s derived as a mean from the semblance analysis of the ultra-long streamer  
246 data (Marjanović et al., 2020). Additional constrains on the sedimentary blanket along IS-01 are  
247 available for the coincident seismic profile of Mehouchi and Singh (2018).

## 248 3.3 OBS Processing



249 The OBS data were corrected for the internal clock drift and were relocated using the symmetry  
250 of the direct wave and a least-squares method (e.g., Creager & Dorman, 1982). The acoustic  
251 sound speed profile of water was obtained by onboard Expendable Bathythermograph (XBT) and  
252 World Ocean Circulation Experiment (WOCE) Conductivity/Temperature/Depth (CTD) data.  
253 The OBS depth was further corrected to match the constrained seafloor depth and a  
254 corresponding time shift was applied to the travel times. In this study, we only use the pressure  
255 components of the OBSs. The processing of the OBS data was carried out with Seismic Unix  
256 (Cohen & Stockwell, 2010) using the same sequence and parameters for both lines. A  
257 Butterworth-bandpass filter from 4-20 Hz was applied to the OBS gathers to filter low and high  
258 frequency noise. Moreover, a predictive deconvolution was applied to suppress some energy of  
259 the bubble reverberations and to facilitate the identification of the wide-angle reflection events.  
260 The shape and length of the wavelet, which is crucial for the performance of the predictive  
261 deconvolution, was obtained using a trace autocorrelation methodology (Yilmaz, 2001).



262 **Figure 2:** Record sections, labelled events and arrival picks for two selected OBS. (a,d) Processed  
 263 receiver gathers of OBS 77 (panel a; LI-02) and OBS 5 (panel c; IS-01) with labelled seismic events. The  
 264 travel time is reduced with 8 km/s. The amplitude is normalized by its maximum and clipped to 10 %.  
 265 The X and Z coordinate represent the along-profile-axis distance and the water depth of the OBS. (b,e)  
 266 The same record sections with travel time picks superimposed where colored dots and error bars illustrate  
 267 the picked arrivals for the three distinct seismic phases (Pg, PmP, Pn; see legend) and their individual pick  
 268 uncertainty. (c,f) Corresponding OBS locations (black inverse triangles), bathymetry and the sediment  
 269 thickness (green area) above the igneous basement (gray area). The OBS of the illustrated receiver gather  
 270 is highlighted. Every fourth OBS is labelled.

271

272

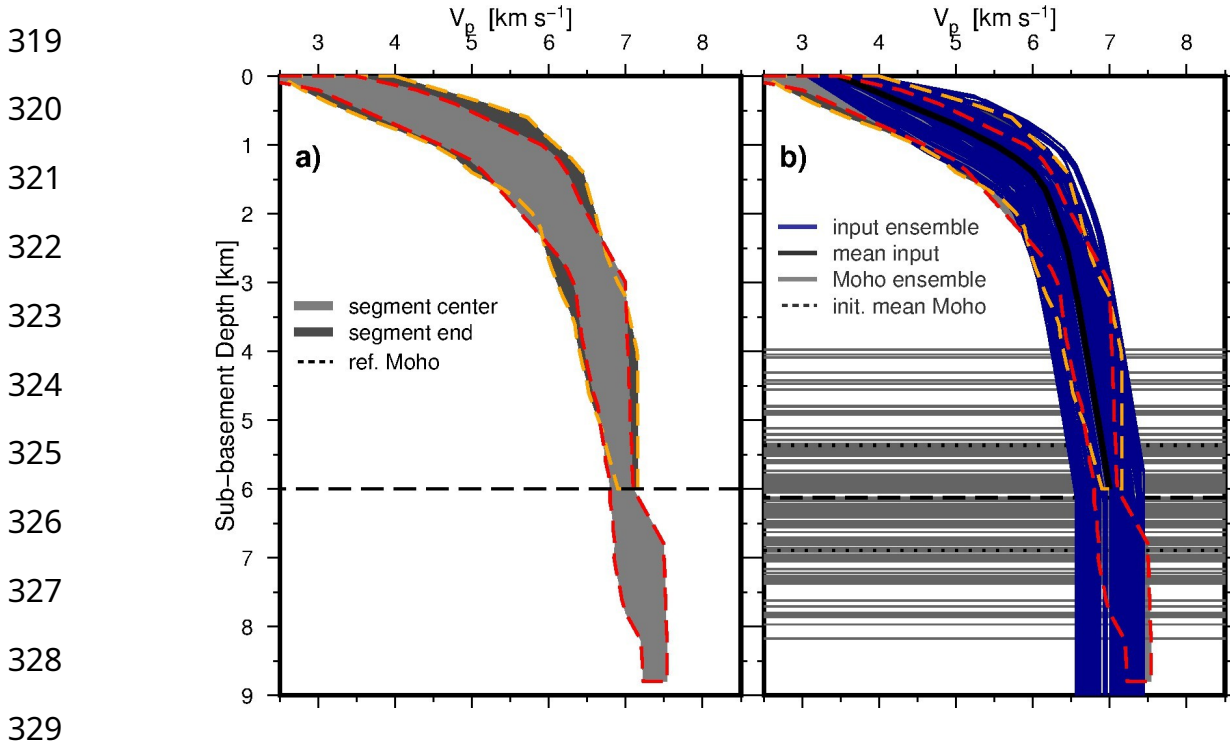
273

## 274 4 Tomographic Traveltime Inversion

275 For the tomographic inversion, a total of  $\sim 10100$  refracted first arrivals (Pg and Pn) and  $\sim 2700$   
 276 wide-angle reflection arrivals (PmP) were manually picked on the 29 receiver gathers (along  
 277 both lines) and an offset-dependent uncertainty was assigned to each pick (e.g., Fig. 2). The  
 278 estimated uncertainties are 30-50 ms for Pg, 70 ms for PmP, and 80-110 ms for Pn arrivals. Both  
 279 the forward modeling and inversion were carried out using the package TOMO2D from  
 280 Korenaga et al. (2000). This code applies a hybrid scheme of the shortest path method from  
 281 Moser (1991) for calculating the least traveltimes between the grid nodes followed by a ray  
 282 bending method (Moser, 1992) to fine-tune these initial ray paths and minimize their travel  
 283 times. The ray bending is thereby conducted using a conjugate gradient method (Moser, 1992).  
 284 For the inverse problem the traveltime residuals for each raypath are equalized with  
 285 perturbations of the velocity and the reflector nodes with respect to a reference model, forming a  
 286 sparse linear system (Korenaga, 2000). Hereinafter, the linear system is normalized by data and  
 287 model covariaces, regularized with smoothing and damping constraints (Korenaga, 2000) and  
 288 can be solved by the sparse matrix solver LSQR (Paige & Saunders, 1982).

289 The model domains were discretized into  $726 \times 141$  (for line LI-02) and  $1167 \times 141$  (for line IS-01)  
 290 cells with a horizontal node spacing of 200 and 300 m, respectively. The larger horizontal node  
 291 spacing for IS-01 was chosen due to the larger shot interval of 300 m. The variable vertical node  
 292 spacing increases with depth from 50 m at the seafloor to 250 m at the bottom of the model.  
 293 Initially, the horizontal and vertical correlation lengths, smoothing, and damping weights that  
 294 regularize the nonlinear inversion were tested and evaluated. Since the seismic velocity generally  
 295 varies more vertically than laterally, smaller vertical than horizontal correlation lengths were  
 296 used, which increased linearly with depth. Based on the smaller shot and receiver spacing and  
 297 hence the higher resolution, slightly smaller correlation lengths were used for the line LI-02.  
 298 Additionally, considering the lower uncertainties of Pg picks, we chose smaller regulation  
 299 weights for the Pg inversion than for the PmP and Pn inversion steps. A 1-D velocity model of  
 300 oceanic crust hung below the constrained sediment/basement interface (Fig. 3) was used as a  
 301 starting velocity model. All parameters of the discretization, forward modelling and inversion are  
 302 also listed in Table S2 in the supplementary material.

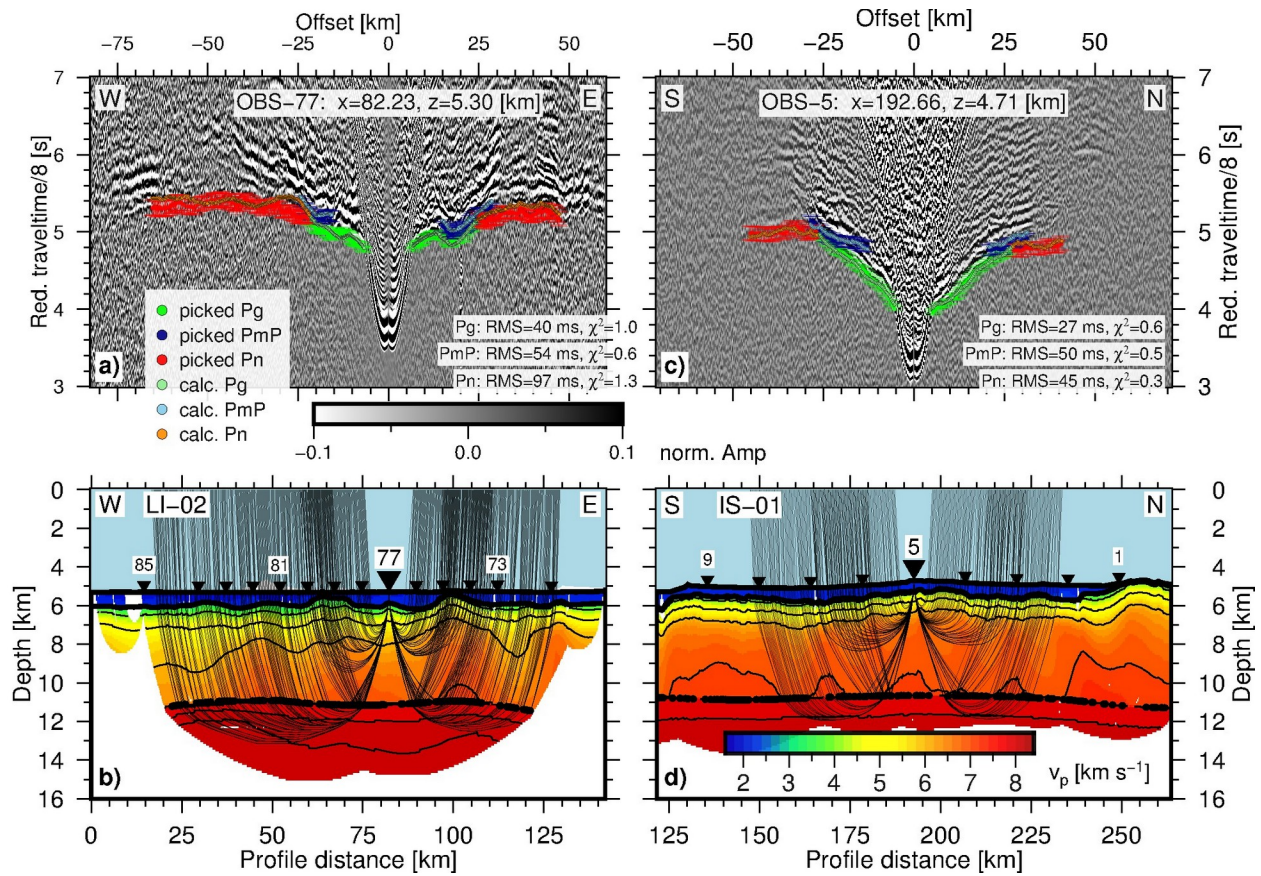
303 The inversion was carried out following a top-to-bottom approach. Hence, first, the near offset  
 304 Pg arrivals were inverted to constrain the shallower upper crust before adding the further offset  
 305 Pg arrivals and inverting again to obtain the velocity structure of the upper and intermediate  
 306 depths of the crust. Thereafter, the PmP reflection arrivals were added and inverted with an initial  
 307 flat Moho reflector with a predefined constant depth (on average 6 km below the mean basement  
 308 depth). The reflector is modeled as a floating reflector with only one degree of freedom  
 309 vertically, and is thus independent from the velocity nodes (Korenaga et al., 2000). A depth  
 310 kernel weighting factor, which controls the tradeoff between the velocity and the reflector depth  
 311 ambiguity from the PmP arrivals (Korenaga et al., 2000) was chosen to be 1 such that velocity  
 312 and reflector depth perturbation are equally weighted. Each iterative inversion stage in the top-  
 313 to-bottom approach is stopped by reaching a normalized target  $\chi^2 \leq 1.2$  or when a maximum  
 314 number of iterations (eight for each Pg segment and PmP) is reached, which results in an  
 315 excellent fit to observed and calculated travel times (Fig. 4). The ray coverage in the model  
 316 domain is represented by the derivative weight sum (DWS; Toomey & Foulger, 1989), which  
 317 incorporates not only the number of rays going through each cell but also their individual path  
 318 length through the cell and their uncertainty.



330 **Figure 3:** Velocity and Moho reflector input ensembles. (a) Reference velocity ensembles and crustal  
 331 thickness obtained for the central portion of the MAR segments (light grey, dashed orange frame) and the  
 332 segment ends (dark grey, dashed red frame) after Grevenmeyer et al. (2018). (b) Randomized input  
 333 velocity (blue) and initial flat Moho (light grey) ensemble for Monte Carlo analysis. Solid, dashed, and  
 334 dotted black lines indicate the mean initial 1D-velocity-depth function, the mean initial flat Moho and its  
 335 standard deviation, respectively.

336 To minimize the bias from the initial model and to evaluate the model uncertainty, a Monte Carlo  
337 analysis (MCA) was performed in which a set of 100 randomized starting velocity models (e.g.,  
338 Fig. 3) and a set of 100 initial flat Moho reflectors of various constant depths were inverted and  
339 averaged to obtain the final crustal model and its standard deviation (see Appendix 1). For the  
340 MCA, the 100 1-D input velocity functions were randomized around a reference velocity  
341 function for the Atlantic crust, which is derived as a mean from a compilation of velocity-depth  
342 profiles from the Atlantic Ocean for ridge segment ends (Grevemeyer et al., 2018; Fig. 3). The  
343 100 initial flat reflectors were randomized around a flat Moho reflector 6 km below the average  
344 basement depth.

345 After obtaining the final average crustal velocity model from the MCA, an initial velocity model  
346 for the upper mantle was added and hung below the mean constrained Moho reflector. To create  
347 the initial 1-D input velocity function for the upper mantle, we observed an apparent velocity of  
348 8 km/s in the Pn arrivals within the data, and reduced this slightly to 7.8 km/s at the Moho depth.  
349 Below the Moho, the mantle velocity increase was defined subsequently by three velocity  
350 gradients: 0.1 s<sup>-1</sup> from 0 to 1 km, 0.05 s<sup>-1</sup> from 1 to 5 km, and 0.04 s<sup>-1</sup> from 5 km to the model  
351 bottom. In the final stage of the entire cumulative inversion scheme, the picked Pn arrivals were  
352 added, and all arrivals were inverted to obtain the final result that included the velocity in the  
353 crust, the Moho reflector, the uppermost mantle (Figs 5 and 6). Due to the high uncertainty of the  
354 Pn picks (80-110 ms) and a previously well constrained final crustal model, a normalized  $\chi^2 \leq 1.2$   
355 was thereby reached after only 2-3 iterations, despite larger damping weights in order to avoid  
356 significant changes within the already constrained crust. The model error is estimated by the  
357 computation of the RMS-fit and the normalized  $\chi^2$ , which incorporates the data variance,  
358 represented by the individual pick uncertainty.



360 **Figure 4:** Traveltime fits and raypaths for two selected OBS. (a,c) Processed receiver gathers of OBS 77  
 361 (panel a) and OBS 5 (panel c) with picked and calculated travel times superimposed and (b,d) their  
 362 corresponding ray paths superimposed on the final velocity models centered at OBS-5 (d) north of and  
 363 OBS-77 (b) within the SPFZ-1. Thick black dots denote the modelled Moho reflection points,  
 364 respectively. The velocity contour interval is 1.0 km/s for the crust, starting with 4 km/s, and 0.1 km/s for  
 365 the mantle, starting at 8.0 km/s. The remaining elements are the same as in Figure 2.

366 To estimate the spatial resolution and the sensitivity of the inversion scheme with respect to the  
367 parametrization of the model space, we conducted multiple checkerboard tests with varying  
368 wavelengths and a velocity perturbation amplitude of 10 % (see Figs. S6 and S7 in the  
369 supplementary material). The results show that anomalies of 25 km horizontal and 5 km vertical  
370 diameter are well resolved with nearly full amplitude for both profiles. Anomalies of 15 km  
371 horizontal and 3 km vertical diameter are only fairly well resolved in the upper to intermediate  
372 crust. In particular, the low velocity anomalies are poorly recovered in the lower crust. We  
373 further tested the resolution of our method in terms of the combination of both an anomalous  
374 sinusoidal Moho reflector, with an oscillating perturbation amplitude of 1 km, and gaussian  
375 velocity anomalies with a perturbation amplitude of 10 %, placed above it in the lower crust. The  
376 results show a very good recovery of the velocity anomalies and a recovery of the anomalous  
377 reflector of ~60-70% (Figs. S8 and S9). Finally, to test the sensitivity within the mantle we  
378 introduced gaussian anomalies with a horizontal diameter of 50 km, a vertical diameter of 3 km  
379 and a perturbation amplitude of 5 % (Figs. S10 and S11) below the constrained Moho reflector.  
380 The results reveal that positive anomalies in the mantle are well resolved up to a perturbation  
381 amplitude of 0.2-0.3 km/s. Conversely, the negative anomalies are with amplitudes up to only 0.1  
382 km/s significantly less recovered. All results of the resolution tests are included in the  
383 supplementary material.

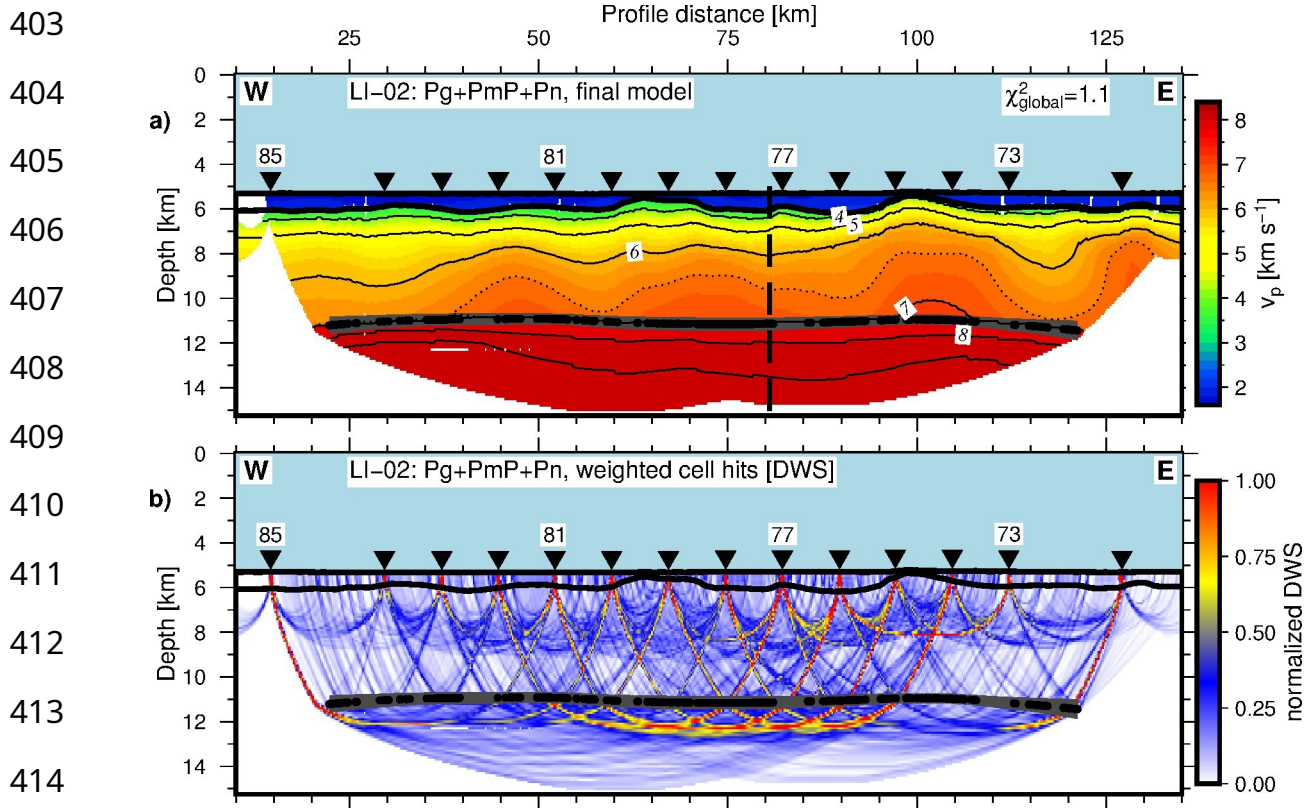
## 384 **5 Tomographic Results**

385 In the following paragraphs the results of the tomographic travel time inversion are presented  
386 separately for the two seismic lines: LI-02 running along the St. Paul fracture zone (Fig. 5) and  
387 IS-01 crossing the St. Paul fracture zone. Note, the results of line IS-01 running north-south (Fig.  
388 6) are subdivided into the distinct areas of north of the SPFZ-1, crossing the SPFZ-1 and south of  
389 the SPFZ-1.

### 390 **5.1 LI-02: Along the St.Paul Fracture Zone**

#### 391 **5.1.1 LI-02: Crustal Seismic Structure along the St.Paul Fracture Zone**

392 The crustal thickness along LI-02 varies from 4.8–5.6±0.3 km, resulting in a mean crust of 5.2  
393 km (Tab. 1 and Fig. 7b). The velocities along the FZ, particularly in the western and central part  
394 of the profile, are remarkably lower in the upper and mid-crust with respect to the reference  
395 model (0.2-0.7 km/s; Fig A1). Along most of the profile, the seismic velocities do not exceed 5  
396 km/s within a sub-basement-depth of 1 km, and the usual seismic layer 3 velocity of ~6.6 km/s  
397 (e.g., Christeson et al., 2019; Grevemeyer et al., 2018) is reached not before 3-4 km depth into  
398 the crust (Figs 5 and 8). However, the eastern part of the profile shows slightly higher velocities  
399 of up to ±0.2 km/s with respect to the reference model and ±0.4-0.8 km/s with respect to the  
400 western part of the profile. Further, these higher velocities (from 90 – 110 km along profile  
401 distance) coincide with a basement high within the FZ (Figs 5 and 7) and thicker crust, indicating  
402 an enhanced magma supply.



415 **Figure 5:** Inversion results for line LI-02. **(a)** Crustal and upper mantle velocity model obtained by  
 416 cumulative Pg, PmP and Pn inversion. The contour interval is 1 km/s in the crust starting at 4 km/s and  
 417 0.1 km/s in the mantle starting at 8.0 km/s. The dotted line represents a usual velocity of the lower crust  
 418 of 6.6 km/s. Black dots and grey shading denote the modelled Moho reflection points and the Moho  
 419 standard deviation, respectively. The vertical dashed line depicts the intersection location with line IS-01  
 420 (Fig. 1b). The remaining elements and symbols are the same as in Figure 4. **(b)** Corresponding  
 421 normalized DWS for the crust and upper mantle.

### 422 5.1.2 LI-02: Upper Mantle Structure along the St. Paul Fracture Zone

423 The Pn inversion yields a rather homogeneous upper mantle with velocities of ~8 km/s along the  
 424 profile LI-02 and hence parallel to the spreading direction (Figs. 5 and 7). Abundant far offset Pn  
 425 arrivals up to 100 km on several OBS gathers provide ray penetration up to 6 km below the  
 426 Moho, and hence a good ray coverage in the upper mantle (Fig. 5). Therefore, these mantle  
 427 velocities are real and not attributable to the initial velocity model.

### 428 5.1.3 LI-02: Uncertainties along the St. Paul Fracture Zone

429 The final computed Pg, PmP, and Pn arrivals yield RMS fits of 46, 56, and 91 ms, respectively,  
 430 and result in a normalized global  $\chi^2$  of 1.1. During the MCA, the standard deviation of the  
 431 velocity model is reduced from 0.3-0.5 km/s to <0.2 km/s in the upper crust and < 0.1 km/s in the  
 432 intermediate and lower crust (Fig. A1). The standard deviation for the Moho reflector depth and  
 433 hence the crustal thickness is reduced from an initial 0.75 km to a mean of 0.3 km. The mean  
 434 values and uncertainties for both crustal thickness and velocities are provided in Table 1.



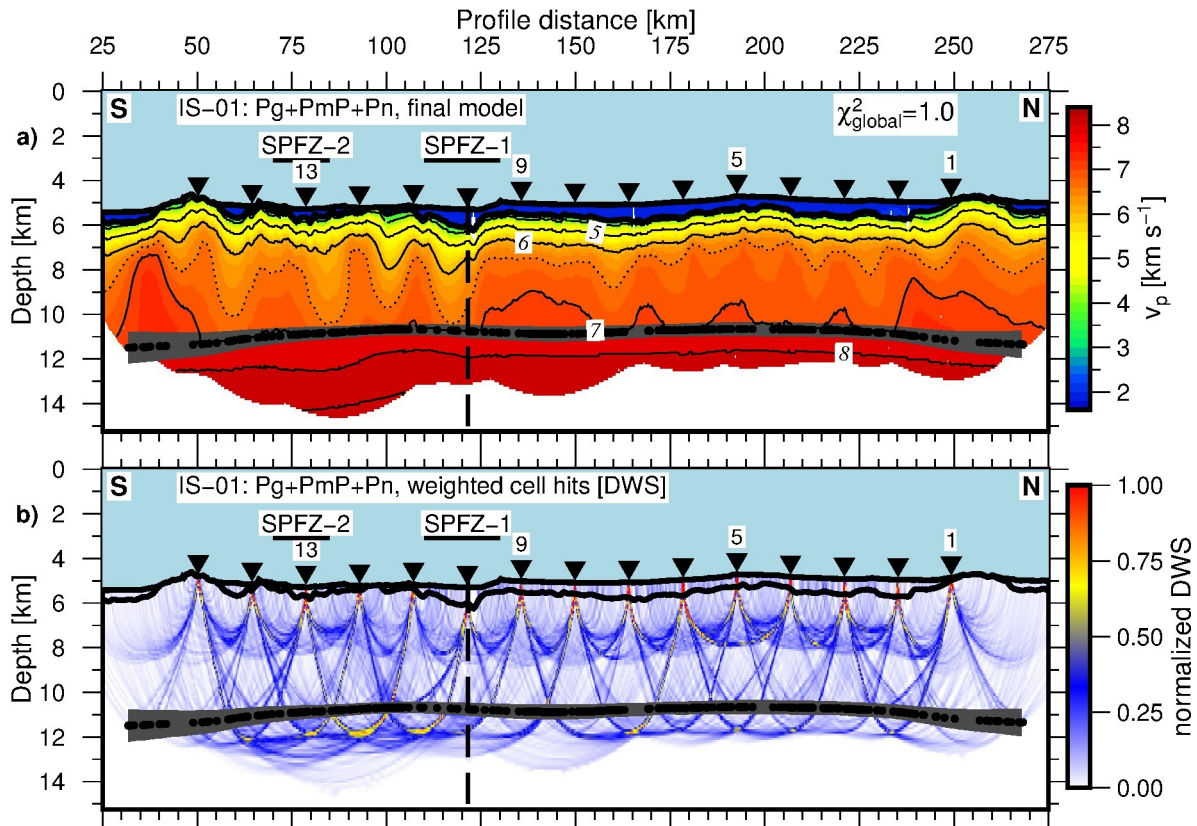
## 435 5.2 IS-01: Across the St. Paul Fracture Zone

## 436 5.2.1 IS-01: North of SPFZ-1

437 The final crustal model for IS-01 reveals a relatively constant crustal thickness along the whole  
438 profile (Figs 6 and 7) but can be subdivided into the two parts: north and south of the SPFZ-1 in  
439 terms of velocity structure. The part north of the FZ encompasses a distance of  $\sim 110$  km (from  
440 130 km to 240 km along profile distance), which displays a crustal thickness of 5.0-5.4 $\pm$ 0.3 km  
441 (mean=5.3 km). A thick crust,  $\sim 6.5\pm 0.5$  km (Fig. 7), is observed at the northern end of the profile  
442 in a 15-20 km wide zone (at distance  $\sim 240$  km), which coincides with a high basement  
443 topography (Figs 6 and 7). However, since the Moho reflector north of  $\sim 240$  km (along profile  
444 distance) is not constrained by reversed ray coverage (Fig. 6), it may not be resolved properly  
445 and is hence excluded from the further interpretation and statistical computations. The velocity  
446 structure north of the FZ is relatively uniform and shows significantly higher crustal velocities  
447 (+0.2-0.6 km/s) with respect to the reference model (Fig. A2).

448 The velocity depth-profiles in this region extracted from the final crustal velocity model (in  
449 Figure 8 marked as o, p, and q) resemble the seismic structure of usual oceanic crust containing  
450 the two-layer gradient structure with a high-velocity gradient in the upper crust and a low-  
451 velocity gradient in the intermediate and lower crust representing mafic layer 2 and the gabbroic  
452 layer 3, respectively (Fig. 8 b, c). Here, layer 2 reveals velocities  $\sim 4$  km/s at the top increasing  
453 to  $\sim 6.2$ - $6.5$  km/s at its base ( $\sim 1.6\pm 0.3$  km sub-basement depth); the velocities of layer 3  
454 increase from  $\sim 6.5$ - $6.7$  km/s at the top of the layer to  $\sim 6.9$ - $7.2$  km/s at the base of the crust.

455 When compared to most of the profiles from LI-02, along the FZ, the layer 2-layer 3 boundary is  
456 more distinctively defined north of St. Paul. Further, crustal velocities are generally higher, with  
457 values of  $\sim 4.5$ - $5$  km/s in the upper crust compared to  $< 3.5$  km/s at the top of the crust along the  
458 FZ, and values of  $> 6.8$  km/s in the lower crust compared to  $\sim 6.3$ - $6.8$  km/s at the base of the crust  
459 along the FZ. However, the eastern domain of LI-02 (profiles d, e in Fig. 8) shows a closer  
460 similarity to the crust north of St. Paul, with a potential layer 2-layer 3 interface of transition  
461 zone occurring at  $\sim 1.7$  km below the basement.



463 **Figure 6:** Inversion results for line IS-01. **(a)** Crustal and upper mantle velocity model obtained by  
 464 cumulative Pg, PmP and Pn inversion. **(b)** Corresponding DWS for the crust and upper mantle. Thick  
 465 horizontal labelled bars indicate the two FZs and their extent derived from the bathymetry (Fig. 1b). The  
 466 remaining figure elements and contour intervals are the same as in Figure 5.

#### 467 5.2.2 IS-01: Across SPFZ-1

468 Across the SPFZ-1 from north to south, the crustal thickness decreases from  $5.2 \pm 0.3$  km to  
 469  $4.8 \pm 0.3$  km (Figs 6 and 7). Within a distance of  $\sim 20$  km from the center of the valley, the crust  
 470 thickens again to  $5.3 \pm 0.4$  km, resulting in a zone of reduced crustal thickness about 20 km-wide  
 471 The FZ exhibits only slightly lower velocities compared to the reference model at segment ends  
 472 (Fig. A2). However, with respect to the adjacent crust in the north of the FZ it reveals a  
 473 remarkable velocity reduction of 0.4-0.8 km/s throughout the upper and mid-crustal region (Fig.  
 474 8c: compare profile n with o, p, q).

## 475 5.2.3 IS-01: South of SPFZ-1

476 The southern part of the profile differs remarkably from the observations in the northern part,  
477 showing more heterogeneities both in crustal thickness and velocities (Figs 6 and 7). The crust  
478 thickens from the FZ southwards from a rather thin crust of  $4.8 \pm 0.3$  km to  $5.6 \pm 0.3$  km within a  
479 distance of  $\sim 60$  km (from 115 km to 55 km along reverse profile distance) and reaches a  
480 maximum thickness of  $6.7 \pm 0.4$  km below another basement high at the southern end of the  
481 profile. However, similarly to the northern limit of the profile, the crustal thickness for distance  
482  $< 55$  km is not very well constrained and hence is not included in the statistical computations and  
483 discussion. The velocity distribution shows both positive and negative anomalies with respect to  
484 the reference model, but the velocities are generally lower than those north of the FZ by 0.2–0.8  
485 km/s (Figs 8 and A2). The strong velocity variations affect both the upper and the lower crust.  
486 Parts of the structure south of St. Paul, for example, the low velocity zone just north of the  
487 SPFZ-2 (profile m in Fig. 8a, c), show a similar range of velocities to the structure along the FZ.  
488 However, they also show a clear division into two layers with a high gradient upper crust and  
489 low gradient mid- to lower-crust (occurring at  $\sim 1.5$  km for profile m), and so cannot be  
490 considered to exhibit the same crustal structure as inside the FZ. Conversely, other sections south  
491 of St. Paul, such as at  $\sim 70$  km along profile (profile l in Fig. 8a,c), show a more similar velocity  
492 structure to the crust north of the FZ.

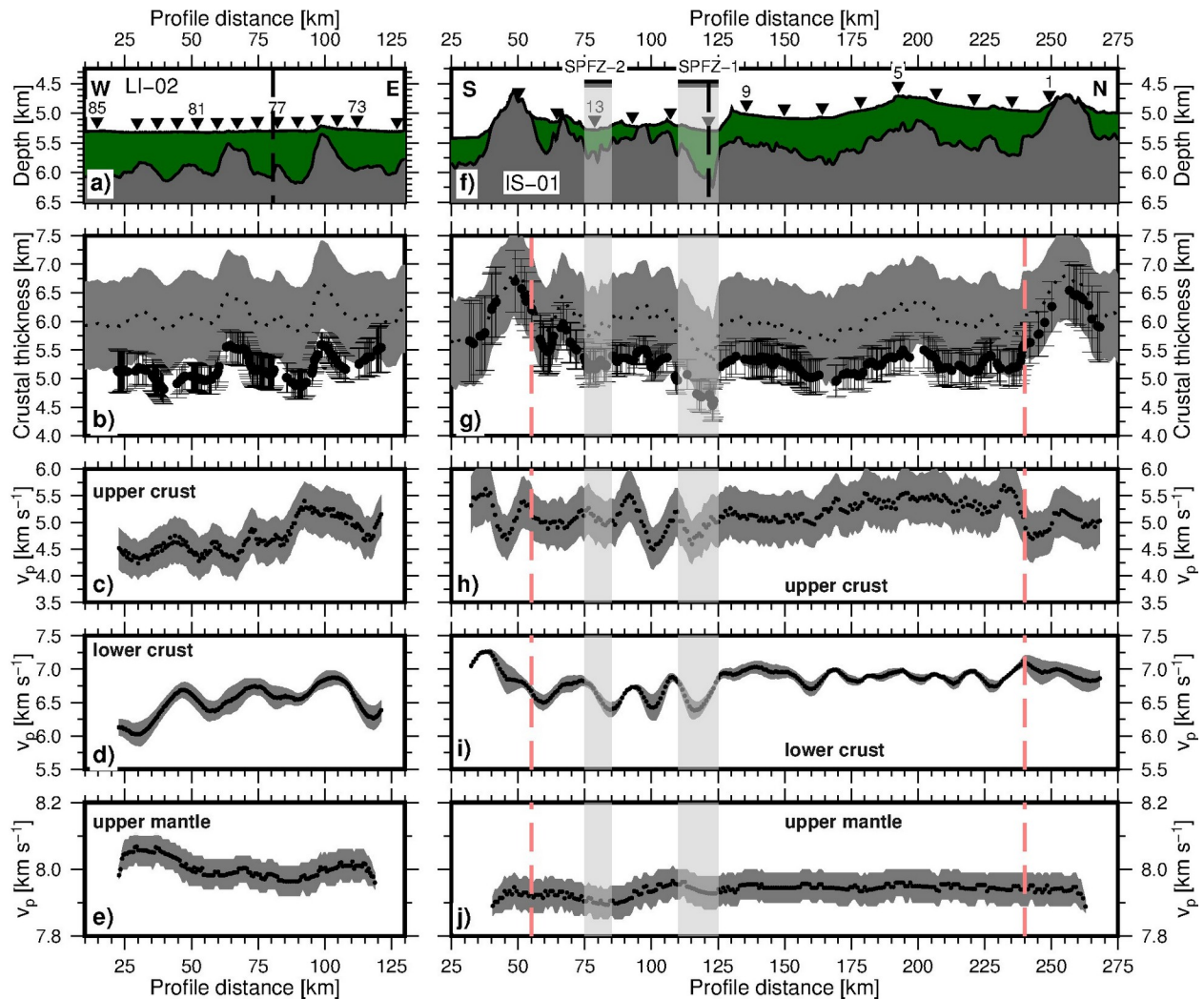
## 493 5.2.4 IS-01: Upper Mantle Structure across SPFZ

494 The Pn inversion yields rather homogeneous upper mantle velocities of 7.8–8 km/s along the  
495 whole profile IS-01 (Figs 6 and 7). Due to a decreasing signal/noise ratio at far offsets in some  
496 record sections and a conservative picking approach of only including picks with uncertainties of  
497  $< 0.12$  s, Pn offsets of good quality were generally limited to offsets smaller than 60 km.

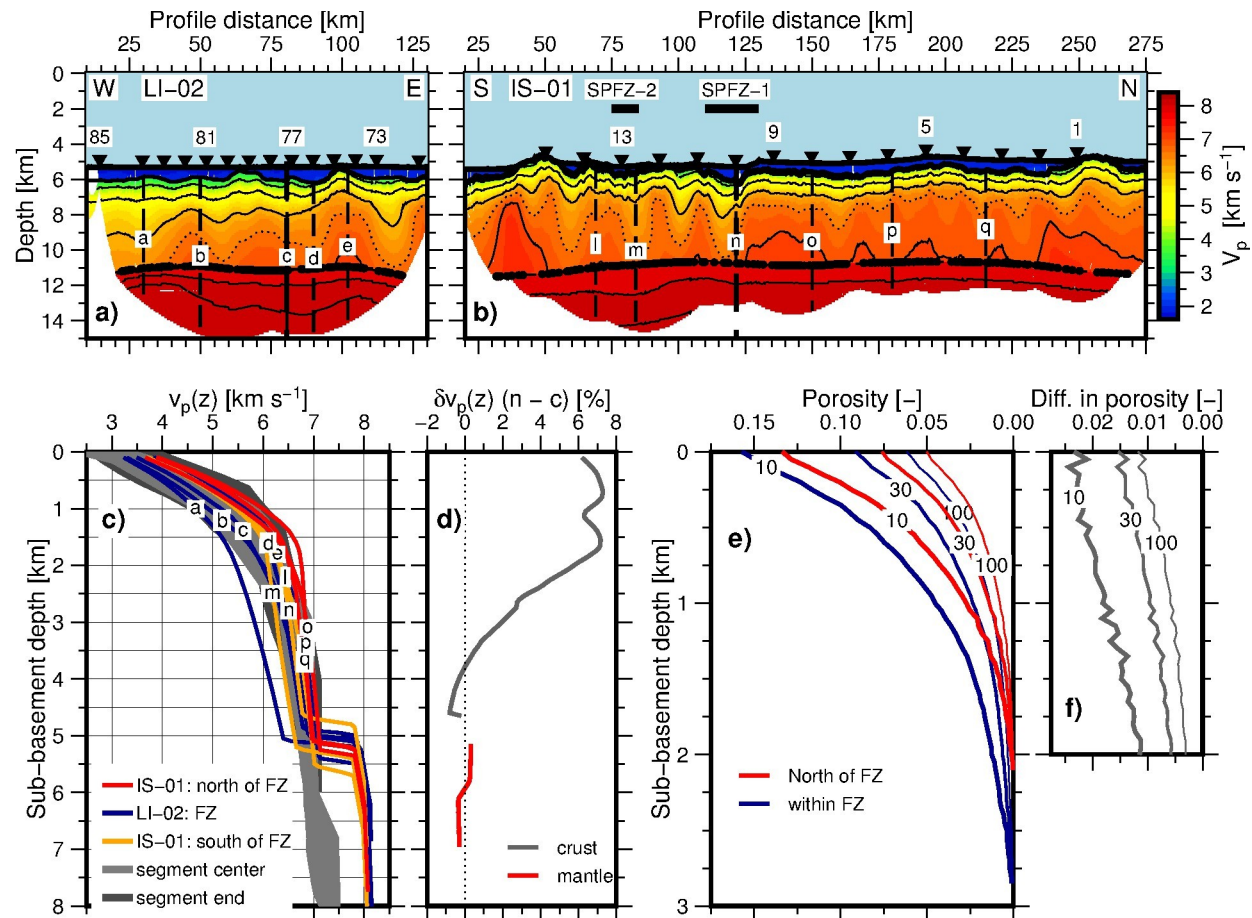
## 498 5.2.5 IS-01: Uncertainties across SPFZ

499 The final computed Pg, PmP, and Pn arrivals yield RMS fits of 41, 67, and 85 ms, respectively,  
500 resulting in a global normalized  $\chi^2 = 1.0$  for both the crustal and the joint crustal and mantle  
501 models. An example of traveltimes fits is illustrated in Figure 4. During the MCA, the velocity  
502 standard deviation was reduced from 0.3–0.5 km/s to  $\sim 0.2$  km/s in the upper crust and  $< 0.1$   
503 km/s in the middle and lower crust (Fig. A2). The significantly higher uncertainty in the shallow  
504 crust is caused by predominantly vertical travel path of the rays and the resulting low sensitivity.  
505 The ray coverage is highest between 1.5–2.0 km of sub-basement depth since this is the depth  
506 where the most rays turn (Fig. 6). Note that beyond the receiver line the crustal velocities are  
507 constrained by only one-sided ray coverage and thus yield a very high uncertainty. The standard  
508 deviation for the Moho reflector depth and hence the crustal thickness north of the FZ, the FZ  
509 itself and south of the FZ is reduced from 0.75 km to 0.3 km. Mean values and uncertainties for  
510 both crustal thickness and velocities are provided in Table 1.

511 5.3 Summary of Results



513 **Figure 7:** Bathymetry, sediment and crustal thickness as well as mean velocities for upper and lower crust  
 514 and upper mantle along both refraction lines (LI-02: panels a-e, IS-01: panels f-j). **(a,f)** Bathymetry,  
 515 sediment thickness (green region) above the basement (gray region) and OBS locations. **(b,g)** Black dots  
 516 with error bars denote the crustal thickness obtained from the modelled Moho reflection points and their  
 517 standard deviation. The dotted line and grey shading denote the mean and standard deviation of the  
 518 crustal thickness input ensemble. **(c-e, h-j)** Vertically averaged velocities for the upper crust (panels c,h;  
 519 0.25 - 1.25 km sub-basement), lower crust (panels d,i; 0.25 -2.5 km above Moho) and the upper mantle  
 520 (panels e,j; 0.25 -1.25 km below Moho) and their corresponding standard deviation (grey shading) along  
 521 the two lines, respectively. Vertical light grey shading indicates the extent of the two fracture zone valleys  
 522 (SPFZ-1,SPFZ-2; Fig. 1). Vertical red dashed line excludes the edge regions that are not constrained by  
 523 reverse ray coverage for IS-01. Remaining elements are the same as in Figure 2 and 5.



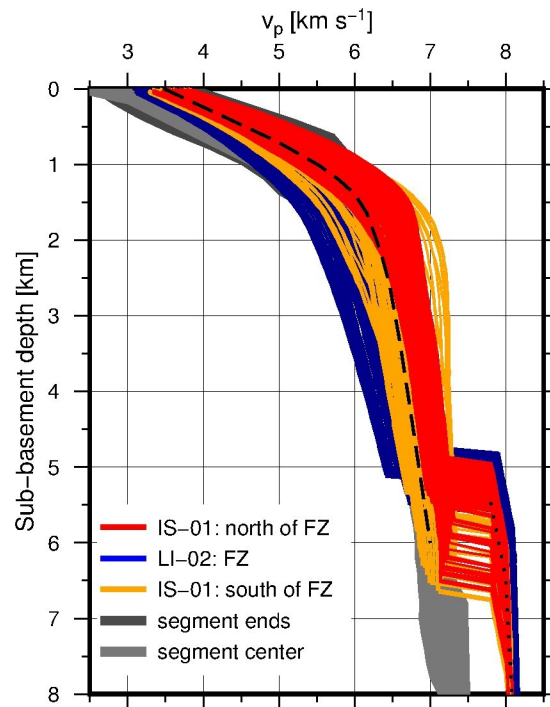
525 **Figure 8:** Velocity and porosity compilation for the two lines. (a,b) The locations for the selected 1-D  
 526 velocity-depth profiles (labelled vertical dashed lines) of line LI-02 (a) and line IS-01 (b) are  
 527 superimposed on the final velocity models. Remaining figure elements are the same as in Figure 5. (c)  
 528 Extracted velocity depth profiles. Each profile represents the average of the velocity-depth profiles for  
 529 four adjacent horizontal nodes. (d) Velocity difference within the vicinity of the profile intersection  
 530 (profile n – profile c). (e) Porosity estimates using DEM analysis for averaged velocity depth functions of  
 531 the SPFZ-1 (averaged from 15 -120 km distance alongside LI-02) and the crust north of it (averaged from  
 532 130 -240 km distance alongside IS-01). The labels indicate different aspect ratios of the fractures. (f)  
 533 Difference in porosity between the crust within the fracture zone and north of it (FZ – North).

534 Table 1 lists the findings of this study regarding crustal and upper mantle properties for three  
 535 distinct regions: north of St. Paul, south of St. Paul, and along the St. Paul FZ itself. The mean  
 536 upper crustal velocity is obtained from averaging vertically and horizontally down from 0.25-  
 537 1.25 km of sub-basement depth. The lower crustal velocity is obtained by vertical and horizontal  
 538 averaging of the 0.25–2.5 km (reversed depth) of the lower crust just above the constrained  
 539 Moho reflector. The mean upper mantle velocity is obtained from vertical and horizontal  
 540 averaging between 0.5-2 km below the constrained Moho reflector. Only regions with sufficient  
 541 ray coverage contribute to these statistical computations. The overall variability of the velocity  
 542 structure in the survey area is also summarized in Figure 9, where 1-D velocity depth profiles are  
 543 extracted for both lines with an interval of three horizontal nodes and colored for the distinct  
 544 regions.

545 Table 1: Summary of the main findings regarding crustal and upper mantle properties.

Parameter / Location	North of FZ	Along FZ	South of FZ
Crustal thickness [km]	$5.3 \pm 0.3$	$5.2 \pm 0.3$	$5.4 \pm 0.3$
Vp upper crust [km/s]	$5.2 \pm 0.5$	$4.7 \pm 0.4$	$5.1 \pm 0.4$
Vp lower crust [km/s]	$6.9 \pm 0.1$	$6.5 \pm 0.1$	$6.7 \pm 0.1$
Vp upper mantle [km/s]	$7.9 \pm 0.05$	$8.0 \pm 0.05$	$7.9 \pm 0.05$

546  
547



548 **Figure 9:** Velocity-depth compilation. The 1-D velocity-depth functions are extracted with an interval of  
549 three horizontal nodes (0.6 km for LI-02 and 0.9 km for IS-01, respectively) and color coded for the  
550 distinct regions (see legend). Grey shading indicates the reference velocity ensemble from Grevenmeyer et  
551 al. (2018). The dashed and dotted lines denote the mean initial velocity-depth function for the crust and  
552 the initial velocity-depth function used below the constrained Moho for the Pn inversion, respectively.

## 553 **6 Discussion**

### 554 6.1 Crustal Thickness along the St. Paul Fracture Zone

555 In the literature the term fracture zone has been loosely used for both the tectonically and  
556 seismically active transform fault offsetting the spreading axis and its inactive fracture zone (e.g.,  
557 Detrick et al., 1993). Here, we will use the term “transform fault” for the active plate boundary  
558 offsetting the spreading axis, while with the term “fracture zone”, we will refer to the inactive  
559 fossil trace where lithosphere of contrasting age meets and subsidence occurs on either side  
560 depending upon their thermal structures (e.g., Menard, 1967; Sandwell, 1984). This clear  
561 separation between the fracture zones and the transform faults are important as recent evidence  
562 suggest that crust accreted along a transform fault might be affected by processes acting at ridge-  
563 transform intersections before it converts into a fracture zone (e.g., Grevenmeyer et al., 2021;  
564 Marjanović et al., 2020).

565 The St. Paul fracture zone reveals an average crustal thickness of  $\sim 5.2$  km, which is roughly 1  
566 km thinner when compared to the global average of normal oceanic crust of 6.15 km thickness  
567 (e.g., Christeson et al., 2019), but close to the thickness of oceanic crust in the equatorial  
568 Atlantic, from  $5.6\text{-}6.0 \pm 0.1$  km (Vaddineni et al., 2021). Interestingly, it did not show any  
569 significant change in the crustal thickness with respect to the crust found either to the north or  
570 south of the FZ. Furthermore, its thickness is in the same order of magnitude as the Chain FZ  
571 (Marjanović et al., 2020) and falls in the range of other FZ surveyed in the Atlantic Ocean, e.g.  
572  $\sim 4.5$  km at Tydeman FZ (e.g., Calvert & Potts, 1985; Potts et al., 1986a),  $\sim 5$  km for the  
573 Mercurius FZ (Peirce et al., 2019). Additionally, Davy et al. (2020) observed a crustal thickness  
574 of  $\sim 6$  km for the Late Cretaceous Marathon FZ. A new compilation of crustal thicknesses of  
575 major Atlantic TF and FZ (Marjanović et al., 2020) indicates thin crust at some transform faults  
576 (2-5 km) whereas most fracture zones have crustal thicknesses in the range of usual oceanic crust  
577 (5-7 km). An exception, however, is the Kane FZ, which shows a significantly thinner crust (2-3  
578 km) (Cormier et al., 1984; Detrick & Purdy, 1980).

579 In general, the thinner crust found along transform faults and fracture zones is clearly consistent  
580 with the concept of focused mantle upwelling along mid-ocean ridges (e.g., Lin et al., 1990;  
581 Tolstoy et al., 1993), supporting magmatically starved conditions acting at transform faults.  
582 Further, geological observations and sampling of rocks from transform valleys at slow- and  
583 ultraslow-spreading ridges often reveals exposed upper mantle rocks near segment ends (e.g.,  
584 Cannat, 1993; Cannat et al., 1995). These observations are consistent with the inferences from  
585 Detrick et al. (1993), suggesting that crust found at both transform faults and fracture zones is  
586 “thin, intensely fractured, and hydrothermally altered basaltic section overlying ultramafics that  
587 are extensively serpentinized in places”. However, the crust within the St. Paul FZ is only  
588 slightly (0.1-0.3 km) thinner when compared to oceanic crust adjacent to the FZ. A gradual  
589 crustal thinning over a distance of several tens of kilometers on either side of a fracture zone or  
590 transform fault, as reported previously for some fracture zones in the North Atlantic (White et al.,  
591 1984), is not observed, neither across the St. Paul FZ as shown in our data nor across the Chain  
592 FZ (Marjanović et al., 2020). One interpretation might be that the crust found along transform  
593 faults may deviate significantly from oceanic crust in fracture zones, as envisioned recently  
594 (Grevemeyer et al., 2021).

595 A similar deduction has been made recently to explain the crustal structure across the Chain FZ.  
596 Marjanović et al. (2020) suggested that lateral dyke propagation along the adjacent spreading  
597 axis into the transform fault augments crust at RTIs. Such a dyke injection is supported by the  
598 presence of J-shaped ridges in the vicinity of RTIs observed in a global study of transform faults  
599 (Grevemeyer et al., 2021). Bathymetric data obtained along the St. Paul FZ reveal a number of  
600 such J-shaped ridges, though ridge tips are often blanketed by sediments (Fig. 1c). Dyking is  
601 possibly controlled by 3-D mantle upwelling as envisioned by Lin et al. (1990) at slow spreading  
602 ridges. At the 21°30'N segment of the MAR, ridge propagation forced by lateral dyking has not  
603 only advanced into the transform domain, but cut through a transform fault, causing its die-off  
604 (Dannowski et al., 2018). We therefore propose that a second phase of RTI magmatic accretion  
605 might be an important process shaping the crust and lithosphere at the proximal end of transform  
606 faults. However, the proposed model is still rather conceptual and thus we cannot rule out that  
607 magma migrates also along the base of crust. A scenario where magma is supplied within the  
608 mantle before intruding into the crust may explain better the layer-2/layer-3 type layered  
609 structure of the crust found along St. Paul than a model where dyking along is governing RTI  
610 magmatism.

611 The occurrence of a second phase of RTI magmatism is supported by geological sampling,  
612 revealing that lithosphere along transform valleys is generally characterized by mantle  
613 exhumation (e.g., Fox et al., 1986; Tucholke & Lin, 1994), while outside corners and fracture  
614 zones are dominated by magmatically accreted basaltic crust (e.g., Karson & Dick, 1984). The  
615 observation that even the floor of a fracture zone valley (Karson & Dick, 1983) is composed of  
616 basaltic rocks supports the interpretation that transform crust is being augmented at RTIs by  
617 magmatism.

618

619

620



621 6.2 Seismic Velocity Structure along St. Paul Fracture Zone

622 Crustal seismic velocities along the SPFZ reveal significantly reduced values when compared to  
 623 the crust north of the FZ. Throughout the upper and middle crust, velocities are reduced by 0.2-  
 624 1.1 km/s. The velocity structure within the FZ, however, still shows the typical features of a two  
 625 layered crustal structure of normal oceanic crust of oceanic crust formed at segment ends (Fig.  
 626 8c), i.e., a high-velocity gradient upper crust and a low-velocity gradient lower crust. This  
 627 decrease in seismic velocity throughout the entire crust might be best explained by the presence  
 628 of large-scale porosity and fracturing of crustal rocks. Nevertheless, the observed layered  
 629 structure closely resembling oceanic crust supports that crust, though fractured, was  
 630 magmatically accreted. Therefore, the crust found along St. Paul FZ differs profoundly from the  
 631 conventional wisdom where crust at discontinuities is generally characterized by basically a  
 632 single layer and thin crust (e.g. Davy et al., 2020). For a mature oceanic crust near  
 633 15°N/55°30'W in the Atlantic Ocean, Davy et al. (2020) suggest that the structure of ridge crest  
 634 discontinuities is controlled by the behavior of adjacent spreading segments. Therefore, crust  
 635 accreted at discontinuities near magmatically starved spreading segments will mimic those  
 636 conditions, while crust formed at transforms or higher-order ridge offsets adjacent to  
 637 magmatically robust segments will reflect magmatically accreted crust. The accretion near St.  
 638 Paul seems to have occurred during a period of constant magma supply from the mantle.

639 In order to estimate the porosities associated with decreasing velocity, we carried out a  
 640 differential effective medium analysis (DEMA) after Taylor and Singh (2002). The DEMA was  
 641 performed for a host rock of basaltic composition and assuming a population of aligned,  
 642 elongate, fluid-filled fractures with aspect ratios (ARs) between 10 and 100 (Supplementary Fig.  
 643 S5). The porosities are computed for laterally averaged 1-D velocity-depth profiles for both  
 644 within the SPFZ-1 (line LI-02, from 25- 120 km along profile distance) and the crust resembling  
 645 normal oceanic crust north of the SPFZ-1 (line IS-01, from 130-240 km along profile distance).  
 646 The results and their deviation for three different ARs (10, 30, 100) are illustrated in Figures 8e  
 647 and 8f. We obtain porosities decreasing from up to ~15% in the top of the crust to ~0 % at sub-  
 648 basement depths at 2.0-2.75 km for an AR of 10. For an AR of 100 in contrast, the porosity is  
 649 reduced from only ~6 % at the top of the basement to ~0 % at depths of 1.5-2 km. Depending  
 650 on the AR the DEMA reveals porosities that are ~2.25 % (AR=10) to 0.5-1 % (AR=100) higher  
 651 for the FZ with respect to the crust north of it (Fig. 8f). A recent study of the crust at the  
 652 Romanche TF indicate that the porosity could be 15% near the seafloor decreasing to 1% at the  
 653 base of the crust (Gregory et al., 2021). If similar porosity was present within the active St. Paul  
 654 TF, the reduced porosity could be explained by combination of lateral dyke injection at the RTI  
 655 (Marjanović et al., 2020) and hydrothermal alteration and mineral precipitation (Audhkhasi &  
 656 Singh, 2019; Grevemeyer et al., 1999) during the early development of the fracture zone.

657 Increased porosity, which in turn causes decreasing seismic velocities, might be related to past  
658 deformation along the shear zone of the transform fault and/or emplacement of crust in a  
659 tectonically dominated environment at RTIs. This observation nurtures previous interpretation  
660 that fracture zones might be formed by hydrothermally altered basaltic and gabbroic sections that  
661 are to some degree fractured and faulted, as envisioned earlier (e.g., Detrick et al., 1993; White et  
662 al., 1984). However, even though crust might be partially altered and fractured, within the St.  
663 Paul FZ the mantle rocks do not seem to consist of extensively serpentinized peridotite. Instead,  
664 the presence of clear PmP reflection arrivals along the FZ valley and a continuous upper mantle  
665 Pn refraction with apparent velocity of  $\sim 8$  km/s support a relatively dry mantle with a low  
666 degree of hydration or even the absence of upper mantle serpentinization along the entire section  
667 of the SPFZ-1. Inverted velocities along LI-02 are in the order of  $\sim 8$  km/s (Fig. 7) and therefore  
668 much faster than mantle velocity of  $<7.5$ - $7.8$  km/s reported for some Atlantic transform faults  
669 (e.g., Detrick et al., 1993; Davy et al. 2020), supporting our interpretation. The dehydration of the  
670 mantle might be caused by the presence of higher temperature and crustal thickening dyke  
671 injection at the RTI, where the transform fault becomes a fracture zone.

### 672 6.3 Crustal Thickness as a Function of Distance across St. Paul Fracture Zone

673 Most previous studies along the axis of the MAR have revealed a strong dependence of crustal  
674 thickness variations along the ridge crest (e.g., Lin et al., 1990) and hence distance to a transform  
675 fault. For example, between 33-35°N of the MAR, Canales et al. (2000), and Hooft et al. (2000)  
676 observed that crustal thickness varies significantly as a function of distance from both the  
677 Oceanographer transform fault and non-transform offsets, showing thick crust at segment centers  
678 (up to 8 km) and thin crust at segments' ends ( $<3$  km). Similar features are observed at the MAR  
679 at 21°N (Dannowski et al., 2011), and 5°S (Planert et al., 2009) and along the ultra-slow  
680 spreading Southwest Indian Ridge at 50°E (Niu et al., 2015), and 66°E (Muller et al., 1999). In  
681 general, crustal thickness at segment ends of slow-spreading ridges is in the order of 4-6 km  
682 thick and at segment centers thickness may increase to 7-9 km (e.g., Grevemeyer et al., 2018). It  
683 is, therefore, remarkable that our north-south profile reveals an almost constant thickness of 5.2-  
684 5.6 km over 100 km from the FZ with no obvious dependence of crustal thickness with distance  
685 to the St. Paul fracture zone at 2°N. Similar features are reported for the MAR in the vicinity of  
686 the Chain fracture zone, where crustal thickness is in the order of 4.6 to 5.9 km, showing no  
687 significant imprint of the transform discontinuity on ridge crest segmentation (Marjanović et al.,  
688 2020).

689 Another interesting feature is that the observed crustal thickness averages  $\sim 5.4$  km along the  
690  $\sim 200$  km long north-south trending profile (IS-01). Farther south, between  $0^\circ$  and  $\sim 3^\circ\text{S}$  around  
691 the Chain FZ, crustal thickness is 4.6-5.9 km (Marjanović et al., 2020) and at  $2^\circ\text{S}$  of the MAR  
692 the crustal thickness ranges from 5.6 to 6.0 km along a 600 km long flow line profile (Vaddineni  
693 et al., 2021). However, Christeson et al. (2020) reported from five ridge parallel profiles at  $31^\circ\text{S}$   
694 a significant crustal thickness variations of 3.6 to 7.0 km for different crustal ages (6-60 Ma), but  
695 an almost constant thickness along each profile and thus for crust of the same age, suggesting  
696 that the equatorial and south Atlantic shows consistently thinner crust when compared to the  
697 average thickness of 7 km reported by White et al. (1992) for the Atlantic. However, we have to  
698 note that that data compiled by White et al. (1992) occurred predominantly in the North Atlantic  
699 with a large number of experiments in the north-western Atlantic where crust is in the order of 7-  
700 8 km (e.g., Purdy, 1983; Minshull et al., 1991), suggesting that previous estimates might be  
701 biased. In contrast, the majority of crustal thickness estimates, either along our profiles or  
702 elsewhere in the equatorial or south Atlantic region, compares well with global estimates of the  
703 global mean crustal thickness (e.g., Chen, 1992; Christeson et al., 2019; Harding et al., 2017; Van  
704 Avendonk et al., 2017), revealing an average global crustal thickness of 6.15 km (Christeson et  
705 al., 2019). Therefore, most observed crustal thickness estimates compare well to predictions from  
706 petrological models, suggesting an average crustal thickness of 6 km emplaced at a normal  
707 mantle temperature of  $1300^\circ\text{C}$  (e.g., McKenzie & Bickle, 1988; Korenaga et al., 2002).  
708 However, slightly reduced crustal thickness in the equatorial Atlantic of  $\sim 5.3$  km between Chain  
709 and Romanche, roughly 6 km north of Romanche (Gregory et al., 2021) and  $<5.5$  km along our  
710 longitudinal profile may supports a cooler mantle underlying the equatorial Atlantic. This  
711 interpretation is supported by the exceptionally low degree of melting of the upper mantle in the  
712 equatorial Atlantic as indicated by the chemical composition of mantle-derived mid-ocean ridge  
713 peridotites and basalts (Bonatti et al., 1993; Dalton et al., 2014) and upper mantle S-wave  
714 velocity (Grevemeyer, 2020; James et al., 2014).

#### 715 6.4 Anisotropy

716 To assess the crustal and mantle anisotropy, the velocity structure from both seismic lines was  
717 compared in the vicinity of their intersection, averaging properties over a roughly 1 km long  
718 section (due to different node spacing we averaged 0.8 km along LI-02 and 1.2 km along IS-01).  
719 Figure 8d shows the velocity structure of the profiles at the intersection. Positive values indicate  
720 faster velocities mapped along line IS-01 running roughly north-south and hence parallel to the  
721 strike of the ridge axis. Anisotropy reaches a maximum of  $\sim 7\%$  in the upper 2 km of the crust  
722 and decreases continuously to zero at a depth of  $\sim 4$  km below the basement and thus may occur  
723 within the sheeted dykes. Within the upper mantle, no significant velocity anisotropy can be  
724 observed.

725 Our observation of the upper to mid-crustal anisotropy indicates higher velocities perpendicular  
 726 to the fracture zone (i.e., along the strike of the ridge) with respect to velocities obtained parallel  
 727 to the fracture zone (i.e., perpendicular to the ridge axis). It is interesting to note that our  
 728 observations are consistent with that at the East Pacific Rise, where 4% of anisotropy was  
 729 observed with the fast direction roughly trending along the strike of the ridge crest (e.g., Dunn &  
 730 Toomey, 2001), which was interpreted to represent the effect of ridge-parallel trending faults. At  
 731 St. Paul, the fast-direction seems also to be orientated parallel to the spreading axis. Therefore, if  
 732 the observed crustal anisotropy would be caused by a set of faults it would support a set of faults  
 733 cutting through FZ. Alternatively, anisotropy could be related to the emplacement of dykes,  
 734 which are the dominant feature at 1 to 3 km depth in oceanic crust. One interpretation might  
 735 therefore be that crustal anisotropy reflects J-shaped ridges migrating into the transform domain.  
 736 However, one has to be careful in interpreting the crustal anisotropy as it is derived from two  
 737 crossing profiles.

738 Another interesting feature is the lack of any apparent upper mantle anisotropy. Gaherty et al.  
 739 (2004) observed 3.4% of upper mantle anisotropy in the North Atlantic to the south of Bermuda  
 740 and in the Pacific mantle anisotropy is a striking feature, with values reaching 6-7% in short  
 741 offset experiments at the East Pacific Rise (Dunn & Toomey, 1997; Dunn et al., 2000).  
 742 Therefore, the absence of any anisotropy is a puzzling feature and it might therefore be  
 743 reasonably to argue that mantle velocity along the fast direction and hence along the fracture  
 744 zone might be with 7.9-8.1 km/s rather low. However, as stresses rotate over a short distance  
 745 when approaching a transform fault (Morgan & Parmentier, 1984), mantle flow might be  
 746 distorted along fracture zones and hence anisotropic pattern. In general, a velocity of ~8 km/s is  
 747 in the range of observations from mature lithosphere when being sampled along ridge parallel  
 748 profile (e.g., Davy et al., 2020; Gaherty et al. 2004) and much lower when compared to, for  
 749 example, a flow line profile at 2°S where Vaddineni et al. (2021) observed in 20 to 30 Myr old  
 750 lithosphere an upper mantle velocity of ~8.2 km/s. Observations obtained from the travel times  
 751 of Pn arrivals of regional earthquakes recorded at moored hydrophones support this discrepancy,  
 752 revealing for equatorial upper mantle a seismic velocity of 7.7 km/s in the slow and 8.4 km/s in  
 753 the fast direction (de Melo et al., 2020). Therefore, it might be reasonably to suggest that some  
 754 small degree of uppermost hydration along SPFZ might be hidden by effects of mantle  
 755 anisotropy.

## 756 **7 Conclusions**

757 We presented new constraints from seismic reflection and wide-angle data surveying the crustal  
 758 and upper mantle structure along and across the St. Paul fracture zone, one of the largest  
 759 transform faults in the equatorial Atlantic Ocean. High-resolution P-wave travel time  
 760 tomography revealed a number of key observations:

761 1.) Crustal structure along the fracture zone shows the typical layering of magmatically  
 762 accreted oceanic crust with a crustal thickness of 5 to 5.5 km, a clearly defined seismic Moho  
 763 and an upper mantle velocity of ~8 km/s.

764 2.) Crustal thickness across the fracture zone is in the order of 5 to 6 km, showing only a few  
765 hundreds of meters of crustal thinning in the vicinity of the St. Paul fracture zone. However,  
766 crust at St. Paul is slightly thinner than anywhere else along the line. Nevertheless, the roughly  
767 200 km long well-resolved part of the fracture zone crossing profile did not show the same  
768 features and strong crustal thickness variation of 2-4 km found along the active Mid-Atlantic  
769 Ridge elsewhere (e.g., Canales et al., 2000; Dannowski et al., 2011; Hooft et al., 2000; Planert et  
770 al., 2009) and thus did not show strong evidence supporting decreased melt production and hence  
771 occurrence of magmatically starved crust at transform faults (e.g., Lin et al., 1990; Tolstoy et al.,  
772 1993).

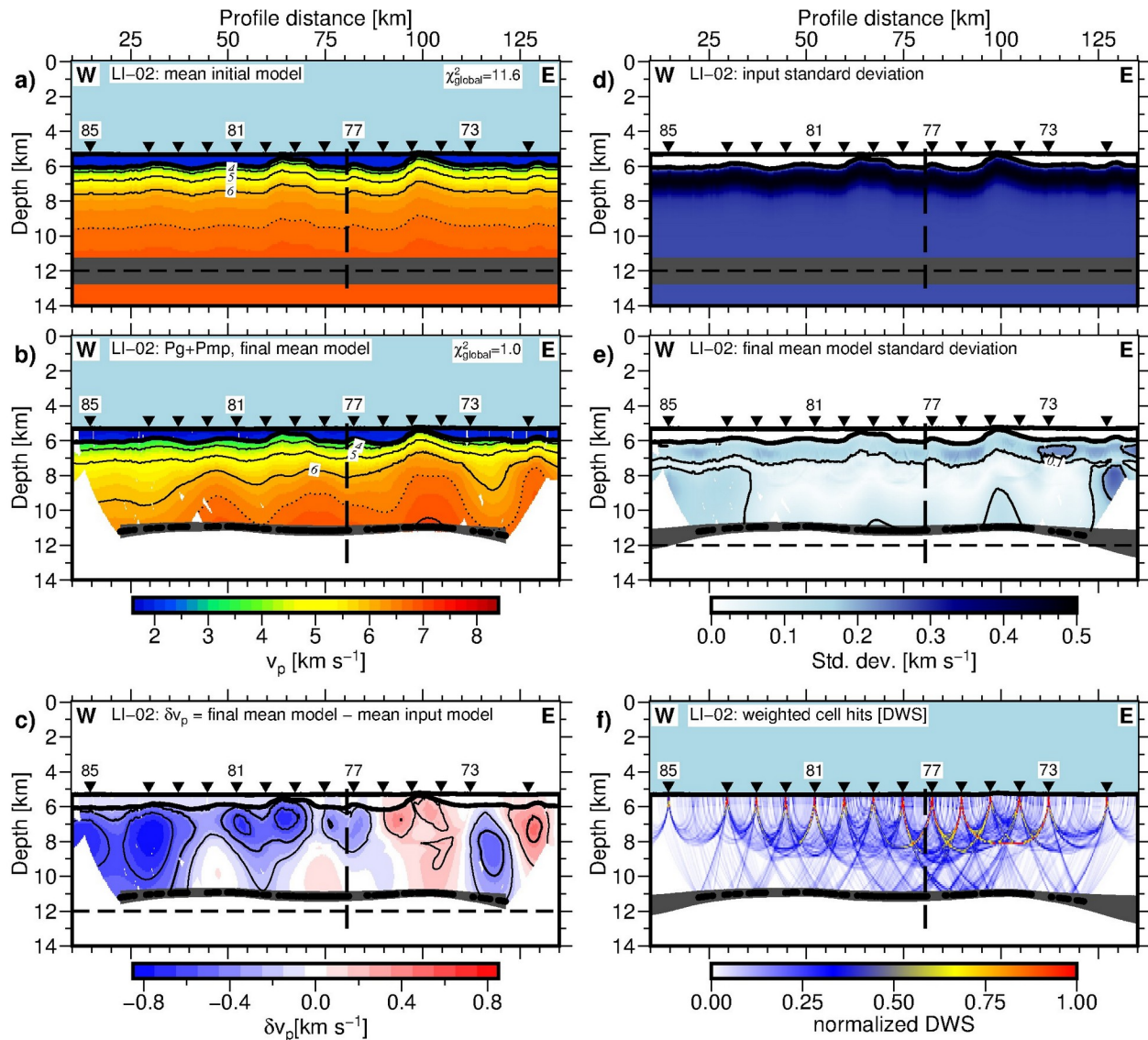
773 3.) Crustal seismic velocities along St. Paul are a few percent slower than farther away from it.  
774 This observation may suggest that crust along the fracture zone has either higher porosity,  
775 probably caused by a larger degree of fracturing, or it may reflect anisotropy. Unfortunately,  
776 anisotropy is poorly resolved in the two crossing profiles.

777 4.) Mantle velocity of  $\sim 8$  km/s along the transform fault did not reveal strong evidence for  
778 serpentinization of the uppermost mantle below the FZ, a feature which has previously been  
779 reported for a number of Atlantic fracture zones (e.g., Detrick et al., 1993) and was interpreted in  
780 terms of highly fracture and hydrated lithosphere. However, with  $\sim 8$  km/s upper mantle velocity  
781 it is only slightly faster along the transform fault that with  $\sim 7.95$  km/s across it, hardly showing  
782 any evidence for a strong mantle anisotropy, which is believed to be an intrinsic feature of the  
783 ocean lithosphere formed by seafloor spreading.

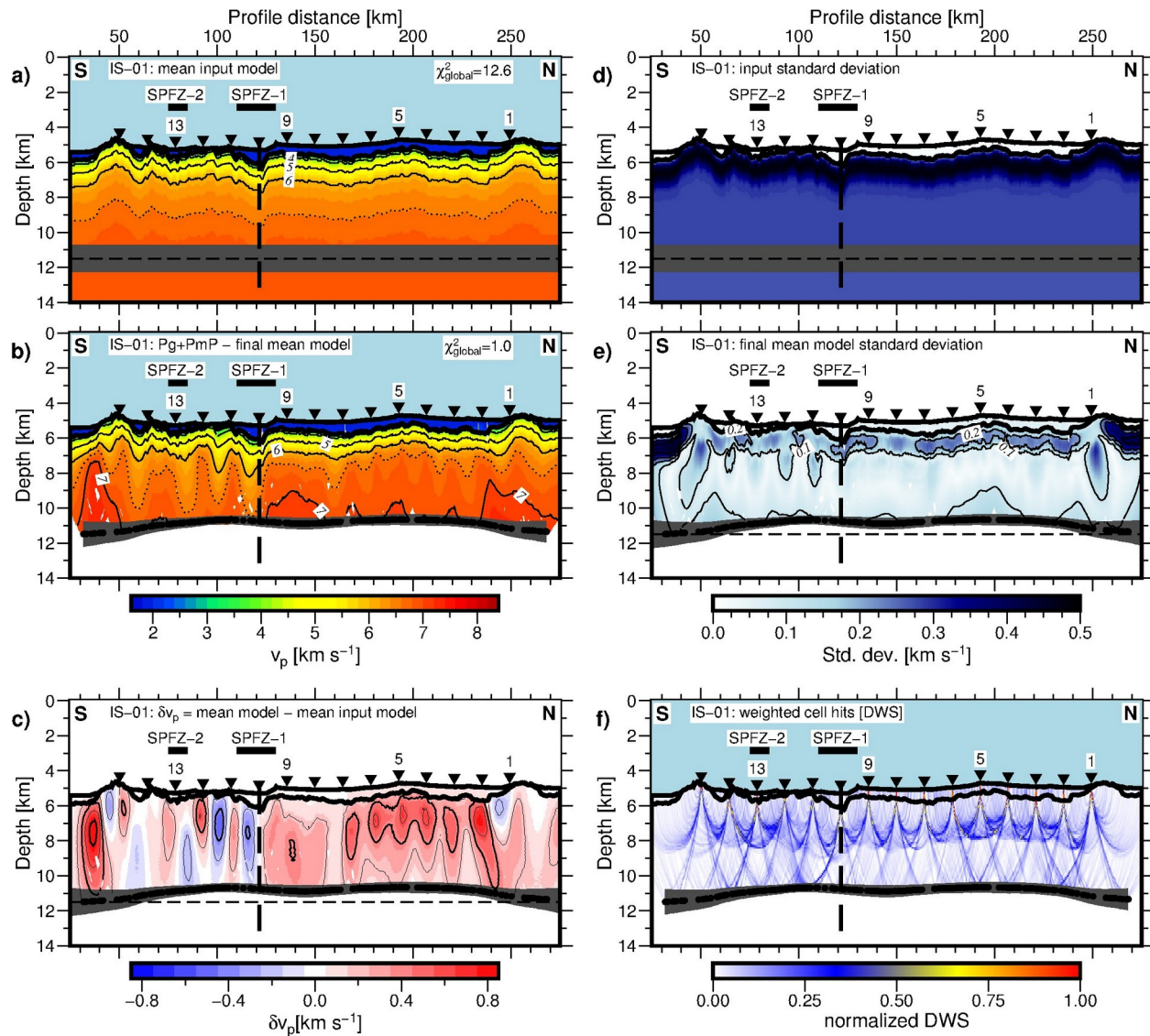
784 We like to interpret our observation with respect to a model where magmatically starved and  
785 tectonically disruptive lithosphere envisioned for transform faults (e.g., Detrick et al., 1993) is  
786 magmatically augmented at the proximal ridge-transform intersection before transform crust is  
787 turning into a fracture zone. Such a scenario has recently been envisioned to explain the fact that  
788 world-wide transform faults are several hundreds of meters deeper than their adjacent fracture  
789 zones and is supported by high-resolution bathymetry, showing a phase of accretion at RTIs  
790 (Grevemeyer et al., 2021). Marjanović et al. (2020) suggested that this phase of accretion is  
791 probably controlled by dyke propagation along the adjacent spreading ridge into the transform  
792 fault domain. Therefore, lithosphere found today in the St. Paul FZ has been magmatically  
793 overprinted while passing along its eastern RTI, explaining why crust along St. Paul FZ reflects  
794 magmatically accreted lithosphere.

795

796 **Appendix**



798 **Figure A1:** Results from Monte Carlo analysis for the line LI-02 along St. Paul FZ (Fig. 1c): **(a)** Mean  
 799 initial crustal velocity model (Grevemeyer et al., 2018). **(b)** Mean final crustal velocity model obtained by  
 800 cumulative inversion of Pg and PmP arrivals. The velocity contour is 1 km/s starting from 4 km/s. **(c)**  
 801 Velocity deviation between mean final and mean initial model (final - initial). The contour interval is 0.2  
 802 km/s starting at 0.2 km/s. **(d)** The initial standard deviation of the mean input velocity model. **(e)** The  
 803 standard deviation of the final mean model. The contour interval is 0.1 km/s. **(f)** Weighted cell hits (DWS)  
 804 of the final mean model. Black dots, horizontal black dashed line and grey shading denote the modelled  
 805 Moho reflection points, the mean initial flat Moho and the Moho standard deviation, respectively. All  
 806 remaining elements are the same as in Figure 5.



808 **Figure A2:** MCA results for line IS-01 across SPFZ (Fig. 1b): All figure elements are the same as in  
 809 Figure A1 and Figure 6.

810 **Acknowledgements**

811 This research was funded by the German Science Foundation (DFG grant MerMET 15-93) and  
 812 the European Research Council under the European Union's Seventh Framework Programme  
 813 (FP7/2007-2013) under Advance Grant agreement no. 339442. We would like to thank captains  
 814 and the crews of the German R/V Maria S. Merian and the French RV Pourquoi-pas? for  
 815 excellent sea-going support, enabling the successful data acquisition. All figures are produced  
 816 with GMT (Wessel et al., 2013). The MCS and OBS data will be made available on the Pangea  
 817 open access data repository upon the acceptance of the manuscript.

818

819 **References**

- 820 Ambos, E.L & Hussong D.M. (1986). Oceanographer transform fault structure compared  
821 to that of surrounding oceanic crust: Results from seismic refraction data analysis.  
822 *Journal of geodynamics*, 5.1, pp. 79–102. [https://doi.org/10.1016/0264-](https://doi.org/10.1016/0264-3707(86)90024-4)  
823 [3707\(86\)90024-4](https://doi.org/10.1016/0264-3707(86)90024-4)
- 824
- 825 Bell, R. E., & Buck, W. R. (1992). Crustal control of ridge segmentation inferred from  
826 observations of the Reykjanes Ridge. *Nature*, 357, 583–586.  
827 <https://doi.org/10.1038/357583a0>
- 828
- 829 Bird, P. (2003). “An updated digital model of plate boundaries”. *Geochemistry,*  
830 *Geophysics, Geosystems*, 4.3. <https://doi.org/10.1029/2001GC000252>
- 831
- 832 Bonatti, E., Seyler, M., & Sushevskaya, N. (1993)., A cold suboceanic mantle belt at the  
833 Earth equator. *Science* 261, 315-320. <https://doi.org/10.1126/science.261.5119.315>
- 834
- 835 Cannat, M. (1993). Emplacement of mantle rocks in the seafloor at mid-ocean ridges,  
836 *Journal of Geophysical Research*, 98, 4163-4172. <https://doi.org/10.1029/92JB02221>
- 837
- 838 Cannat, M., Mevel, C., Maia, M., Deplus, C., Durand, C., Gente, P., Agrinier, P.,  
839 Belarouchi, A., Dubuisson, G., Humler, E., & Reynolds, J.(1995). Thin crust,  
840 ultramafic exposures, and rugged faulting patterns at the Mid-Atlantic Ridge (22–24°  
841 N), *Geology* 23, 49-52. [https://doi.org/10.1130/0091-](https://doi.org/10.1130/0091-7613(1995)023<0049:TCUEAR>2.3.CO;2)  
842 [7613\(1995\)023<0049:TCUEAR>2.3.CO;2](https://doi.org/10.1130/0091-7613(1995)023<0049:TCUEAR>2.3.CO;2)
- 843
- 844 Carlson, R. L., & Miller, D. J. (2004). Influence of pressure and mineralogy on seismic  
845 velocities in oceanic gabbros: Implications for the composition and state of the lower



846 oceanic crust, *Journal of Geophysical Research*, 109, B09205.

847 <https://doi.org/10.1029/2003JB002699>

848

849 Calvert, A.J., & Potts, C.G. (1985). Seismic evidence for hydrothermally altered mantle

850 beneath old crust in the Tydeman fracture zone. *Earth and Planetary Science Letters*,

851 75.4, pp. 439–449. [https://doi.org/10.1016/0012-821X\(85\)90187-6](https://doi.org/10.1016/0012-821X(85)90187-6)

852

853 Canales, J. P., Detrick, R. S., Lin, J., Collins, J. A., & Toomey, D. R. (2000). Crustal and

854 upper mantle seismic structure beneath the rift mountains and across a nontransform

855 offset at the Mid-Atlantic Ridge (35 N). *Journal of Geophysical Research: Solid Earth*,

856 105(B2), 2699–2719. <https://doi.org/10.1029/1999JB900379>

857

858 Chen, Y. J. (1992). Oceanic crustal thickness versus spreading rate. *Geophysical Research*

859 *Letters*, 19(8), 753–756. <https://doi.org/10.1029/92GL00161>

860

861 Christeson, G. L., Goff, J. A., & Reece, R. S. (2019). Synthesis of oceanic crustal structure

862 from two-dimensional seismic profiles. *Reviews of Geophysics*, 57, 504–529.

863 <https://doi.org/10.1029/2019RG000641>

864

865 Christeson, G. L., Reece, R. S., Kardell, D. A., Estep, J. D., Fedotova, A., & Goff, J. A.

866 (2020). South Atlantic Transect: Variations in Oceanic Crustal Structure at 31° S.

867 *Geochemistry, Geophysics, Geosystems*, 21(7), e2020GC009017.

868 <https://doi.org/10.1029/2020GC009017>

869

870 Cohen, J.K. , Stockwell, J.W. (2010). CWP/SU: Seismic Unix Release 41: A free package

871 for seismic research and processing: Center for Wave Phenomena, Colorado School of

872 Mines. Available online at <https://wiki.seismic-unix.org/>

873

874 Cormier, M. H., Detrick, R. S., & Purdy, G. M. (1984). Anomalously thin crust in oceanic  
875 fracture zones: New seismic constraints from the Kane fracture zone. *Journal of*  
876 *Geophysical Research: Solid Earth*, 89(B12), 10249-10266.

877 <https://doi.org/10.1029/JB089iB12p10249>

878

879 Creager, K. C., & Dorman, L. M. (1982). Location of instruments on the seafloor by joint  
880 adjustment of instrument and ship positions. *Journal of Geophysical Research: Solid*  
881 *Earth*, 87(B10), 8379-8388. <https://doi.org/10.1029/JB087iB10p08379>

882

883 Dalton, C. A., Langmuir, C. H., & Gale, A. (2014). Geophysical and geochemical  
884 evidence for deep temperature variations beneath mid-ocean ridges. *Science*,  
885 344(6179), 80-83. <https://www.doi.org/10.1126/science.1249466>

886

887 Dannowski, A., Grevemeyer, I., Phipps Morgan, J., Ranero, C. R., Maia, M., & Klein, G.  
888 (2011). Crustal structure of the propagating TAMMAR ridge segment on the Mid-  
889 Atlantic Ridge, 21.5 N. *Geochemistry, Geophysics, Geosystems*, 12(7).

890 <https://doi.org/10.1029/2011GC003534>

891

892 Dannowski, A., Morgan, J. P., Grevemeyer, I., & Ranero, C. R. (2018). Enhanced mantle  
893 upwelling/melting caused segment propagation, oceanic core complex die off, and the  
894 death of a transform fault: The Mid-Atlantic Ridge at 21.5 N. *Journal of Geophysical*  
895 *Research: Solid Earth*, 123(2), 941-956. <https://doi.org/10.1002/2017JB014273>

896

897 Davy, R. G., Collier, J. S., Henstock, T. J., VoiLA Consortium, Rietbrock, A., Goes, S., et  
898 al. (2020). Wide-angle seismic imaging of two modes of crustal accretion in mature

- 899 Atlantic Ocean crust. *Journal of Geophysical Research: Solid Earth*, 125(6),  
900 e2019JB019100. <https://doi.org/10.1029/2019JB019100>
- 901
- 902 de Melo, G. W., Parnell-Turner, R., Dziak, R. P., Smith, D. K., Maia, M., do Nascimento,  
903 A. F., & Royer, J. Y. (2021). Uppermost Mantle Velocity beneath the Mid-Atlantic  
904 Ridge and Transform Faults in the Equatorial Atlantic Ocean. *Bulletin of the*  
905 *Seismological Society of America*, 111(2), 1067-1079.  
906 <https://doi.org/10.1785/0120200248>
- 907
- 908 Detrick Jr, R. S., & Purdy, G. M. (1980). The crustal structure of the Kane fracture zone  
909 from seismic refraction studies. *Journal of Geophysical Research: Solid Earth*, 85(B7),  
910 3759-3777. <https://doi.org/10.1029/JB085iB07p03759>
- 911
- 912 Detrick, R. S., Cormier, M. H., Prince, R. A., Forsyth, D. W., & Ambos, E. L. (1982).  
913 Seismic constraints on the crustal structure within the Vema fracture zone. *Journal of*  
914 *Geophysical Research: Solid Earth*, 87(B13), 10599-10612.  
915 <https://doi.org/10.1029/JB087iB13p10599>
- 916
- 917 Detrick, R. S., White, R. S., & Purdy, G. M. (1993). Crustal structure of North Atlantic  
918 fracture zones. *Reviews of Geophysics*, 31(4), 439-458.  
919 <https://doi.org/10.1029/93RG01952>
- 920
- 921 Dunn, R. A., & Toomey, D. R. (1997). Seismological evidence for three-dimensional melt  
922 migration beneath the East Pacific Rise. *Nature*, 388(6639), 259-262.  
923 <https://doi.org/10.1038/40831>
- 924

- 925       Dunn, R. A., & Toomey, D. R. (2001). Crack-induced seismic anisotropy in the oceanic  
926       crust across the East Pacific Rise (9° 30' N). *Earth and Planetary Science Letters*,  
927       189(1-2), 9-17. [https://doi.org/10.1016/S0012-821X\(01\)00353-3](https://doi.org/10.1016/S0012-821X(01)00353-3)
- 928
- 929       Dunn, R. A., Toomey, D. R., & Solomon, S. C. (2000). Three-dimensional seismic  
930       structure and physical properties of the crust and shallow mantle beneath the East  
931       Pacific Rise at 9° 30'N. *Journal of Geophysical Research: Solid Earth*, 105(B10),  
932       23537-23555. <https://doi.org/10.1029/2000JB900210>
- 933
- 934       Gaherty, J. B., Lizarralde, D., Collins, J. A., Hirth, G., & Kim, S. (2004). Mantle  
935       deformation during slow seafloor spreading constrained by observations of seismic  
936       anisotropy in the western Atlantic. *Earth and Planetary Science Letters*, 228(3-4), 255-  
937       265. <https://doi.org/10.1016/j.epsl.2004.10.026>
- 938
- 939       Gregory, E., Singh, S. C., Marjanović, M., & Wang, Z. (2021). Serpentinized peridotite  
940       versus thick mafic crust at the Romanche oceanic transform fault, *Geology*, in press
- 941
- 942       Grevemeyer, I. (2020). Upper Mantle Structure beneath the Mid-Atlantic Ridge from  
943       Regional Waveform Modeling. *Bulletin of the Seismological Society of America*,  
944       110(1), 18-25. <https://doi.org/10.1785/0120190080>
- 945
- 946       Grevemeyer, I., Kaul, N., Villinger, H., & Weigel, W. (1999). Hydrothermal activity and  
947       the evolution of the seismic properties of upper oceanic crust. *Journal of Geophysical*  
948       *Research: Solid Earth*, 104(B3), 5069-5079. <https://doi.org/10.1029/1998JB900096>
- 949
- 950       Grevemeyer, I., Ranero, C. R., & Ivandic, M. (2018). Structure of oceanic crust and  
951       serpentinization at subduction trenches. *Geosphere*, 14(2), 395-418.  
952       <https://doi.org/10.1130/GES01537.1>

953

954 Grevemeyer, I., Rüpke, L.H., Morgan, J.P., Iyer, K., & Devey, C.W. (2021). Extensional  
955 tectonics and two-stage crustal accretion at oceanic transform faults. *Nature*, 591, 402–  
956 407. <https://doi.org/10.1038/s41586-021-03278-9>

957

958 Grion, S., Exley, R., Manin, M., Miao, X., Pica, A. L., Wang, Y., et al. (2007). Mirror  
959 imaging of OBS data. *first break*, 25(11). <https://doi.org/10.3997/1365-2397.2007028>

960

961 Harding, J. L., Van Avendonk, H. J., Hayman, N. W., Grevemeyer, I., Peirce, C., &  
962 Dannowski, A. (2017). Magmatic-tectonic conditions for hydrothermal venting on an  
963 ultraslow-spread oceanic core complex. *Geology*, 45(9), 839-842.  
964 <https://doi.org/10.1130/G39045.1>

965

966 Hooft, E. E. E., Detrick, R. S., Toomey, D. R., Collins, J. A., & Lin, J. (2000). Crustal  
967 thickness and structure along three contrasting spreading segments of the Mid-Atlantic  
968 Ridge, 33.5–35 N. *Journal of Geophysical Research: Solid Earth*, 105(B4), 8205-8226.  
969 <https://doi.org/10.1029/1999JB900442>

970

971 James, E. K., Dalton, C. A., & Gaherty, J. B. (2014). Rayleigh wave phase velocities in  
972 the Atlantic upper mantle. *Geochemistry, Geophysics, Geosystems*, 15(11), 4305-4324.  
973 <https://doi.org/10.1002/2014GC005518>

974

975 Korenaga, J., Holbrook, W. S., Kent, G. M., Kelemen, P. B., Detrick, R. S., Larsen, H. C.,  
976 et al. (2000). Crustal structure of the southeast Greenland margin from joint refraction  
977 and reflection seismic tomography. *Journal of Geophysical Research: Solid Earth*,  
978 105(B9), 21591-21614. <https://doi.org/10.1029/2000JB900188>

979

- 980 Korenaga, J., Kelemen, P. B., & Holbrook, W. S. (2002). Methods for resolving the origin  
981 of large igneous provinces from crustal seismology. *Journal of Geophysical Research:  
982 Solid Earth*, 107(B9), ECV-1. <https://doi.org/10.1029/2001JB001030>  
983
- 984 Lin, J., Purdy, G. M., Schouten, H., Sempere, J. C., & Zervas, C. (1990). Evidence from  
985 gravity data for focused magmatic accretion along the Mid-Atlantic Ridge. *Nature*,  
986 344(6267), 627-632. <https://doi.org/10.1038/344627a0>  
987
- 988 Lin, J., & Morgan, J. P. (1992). The spreading rate dependence of three-dimensional mid-  
989 ocean ridge gravity structure. *Geophysical Research Letters*, 19(1), 13-16.  
990 <https://doi.org/10.1029/91GL03041>  
991
- 992 Macdonald, K. C., Fox, P. J., Perram, L. J., Eisen, M. F., Haymon, R. M., Miller, S. P., et  
993 al. (1988). A new view of the mid-ocean ridge from the behaviour of ridge-axis  
994 discontinuities. *Nature*, 335(6187), 217-225. <https://doi.org/10.1038/335217a0>  
995
- 996 Maia, M., Sichel, S., Briais, A., Brunelli, D., Ligi, M., Ferreira, N., et al. (2016). Extreme  
997 mantle uplift and exhumation along a transpressive transform fault. *Nature Geoscience*,  
998 9(8), 619-623. <https://doi.org/10.1038/ngeo2759>  
999
- 1000 Marjanović, M., Singh, S. C., Gregory, E. P., Grevemeyer, I., Grawe, K., Wang, Z., et al.  
1001 (2020). Seismic crustal structure and morphotectonic features associated with the  
1002 Chain Fracture Zone and their role in the evolution of the equatorial Atlantic region.  
1003 *Journal of Geophysical Research: Solid Earth*, 125(10), e2020JB020275.  
1004 <https://doi.org/10.1029/2020JB020275>  
1005

- 1006 Matthews, K. J., Müller, R. D., Wessel, P., & Whittaker, J. M. (2011). The tectonic fabric  
1007 of the ocean basins. *Journal of Geophysical Research: Solid Earth*, 116(B12).  
1008 <https://doi.org/10.1029/2011JB008413>
- 1009
- 1010 McKenzie, D. P., & Parker, R. L. (1967). The North Pacific: an example of tectonics on a  
1011 sphere. *Nature*, 216(5122), 1276-1280. <https://doi.org/10.1038/2161276a0>
- 1012
- 1013 Mckenzie, D. A. N., & Bickle, M. J. (1988). The volume and composition of melt  
1014 generated by extension of the lithosphere. *Journal of petrology*, 29(3), 625-679.  
1015 <https://doi.org/10.1093/petrology/29.3.625>
- 1016
- 1017 Mehouchi, F., & Singh, S. C. (2018). Water-rich sublithospheric melt channel in the  
1018 equatorial Atlantic Ocean. *Nature Geoscience*, 11(1), 65-69.  
1019 <https://doi.org/10.1038/s41561-017-0034-z>
- 1020
- 1021 Menard, H. W. (1967). Extension of northeastern-Pacific fracture zones. *Science*,  
1022 155(3758), 72-74. <https://doi.org/10.1126/science.155.3758.72>
- 1023
- 1024 Menard, H. W. (1955). Deformation of the northeastern Pacific basin and the west coast of  
1025 North America. *Geological Society of America Bulletin*, 66(9), 1149-1198.  
1026 [https://doi.org/10.1130/0016-7606\(1955\)66\[1149:DOTNPB\]2.0.CO;2](https://doi.org/10.1130/0016-7606(1955)66[1149:DOTNPB]2.0.CO;2)
- 1027
- 1028 Minshull, T. A., White, R. S., Mutter, J. C., Buhl, P., Detrick, R. S., Williams, C. A., &  
1029 Morris, E. (1991). Crustal structure at the Blake Spur fracture zone from expanding  
1030 spread profiles. *Journal of Geophysical Research: Solid Earth*, 96(B6), 9955-9984.  
1031 <https://doi.org/10.1029/91JB00431>
- 1032

- 1033 Morgan, W. J. (1968). Rises, trenches, great faults, and crustal blocks. *Journal of*  
1034 *Geophysical Research*, 73(6), 1959-1982. <https://doi.org/10.1029/JB073i006p01959>
- 1035
- 1036 Morgan, J. P., & Parmentier, E. M. (1984). Lithospheric stress near a ridge-transform  
1037 intersection. *Geophysical Research Letters*, 11(2), 113-116.  
1038 <https://doi.org/10.1029/GL011i002p00113>
- 1039
- 1040 Moser, T. J. (1991). Shortest path calculation of seismic rays. *Geophysics*, 56(1), 59-67.  
1041 <https://doi.org/10.1190/1.1442958>
- 1042
- 1043 Moser, T. J., Nolet, G., & Snieder, R. (1992). Ray bending revisited. *Bulletin of the*  
1044 *Seismological Society of America*, 82(1), 259-288.
- 1045
- 1046 Müller, R. D., Sdrolias, M., Gaina, C., & Roest, W. R. (2008). Age, spreading rates, and  
1047 spreading asymmetry of the world's ocean crust. *Geochemistry, Geophysics,*  
1048 *Geosystems*, 9(4). <https://doi.org/10.1029/2007GC001743>
- 1049
- 1050 Muller, M. R., Minshull, T. A., & White, R. S. (1999). Segmentation and melt supply at  
1051 the Southwest Indian Ridge. *Geology*, 27(10), 867-870. [https://doi.org/10.1130/0091-](https://doi.org/10.1130/0091-7613(1999)027<0867:SAMSAT>2.3.CO;2)  
1052 [7613\(1999\)027<0867:SAMSAT>2.3.CO;2](https://doi.org/10.1130/0091-7613(1999)027<0867:SAMSAT>2.3.CO;2)
- 1053
- 1054 Niu, X., Ruan, A., Li, J., Minshull, T. A., Sauter, D., Wu, Z., et al. (2015). Along-axis  
1055 variation in crustal thickness at the ultraslow spreading S outhwest I ndian R idge (50°  
1056 E) from a wide-angle seismic experiment. *Geochemistry, Geophysics, Geosystems*,  
1057 *16(2)*, 468-485. <https://doi.org/10.1002/2014GC005645>
- 1058



- 1059 Paige, C. C., & Saunders, M. A. (1982). LSQR: An algorithm for sparse linear equations  
1060 and sparse least squares. *ACM Transactions on Mathematical Software (TOMS)*, 8(1),  
1061 43-71.
- 1062
- 1063 Peirce, C., Reveley, G., Robinson, A. H., Funnell, M. J., Searle, R. C., Simão, N. M., et al.  
1064 (2019). Constraints on crustal structure of adjacent OCCs and segment boundaries at  
1065 13° N on the Mid-Atlantic Ridge. *Geophysical Journal International*, 217(2), 988-  
1066 1010. <https://doi.org/10.1093/gji/ggz074>
- 1067
- 1068 Planert, L., Flueh, E. R., & Reston, T. J. (2009). Along-and across-axis variations in  
1069 crustal thickness and structure at the Mid-Atlantic Ridge at 5 S obtained from wide-  
1070 angle seismic tomography: Implications for ridge segmentation. *Journal of*  
1071 *Geophysical Research: Solid Earth*, 114(B9). <https://doi.org/10.1029/2008JB006103>
- 1072
- 1073 Potts, C. G., Calvert, A. J., & White, R. S. (1986). Crustal structure of Atlantic fracture  
1074 zones-III. The Tydeman fracture zone. *Geophysical Journal International*, 86(3), 909-  
1075 942. <https://doi.org/10.1111/j.1365-246X.1986.tb00668.x>
- 1076
- 1077 Purdy, G. M. (1983). The seismic structure of 140 Myr old crust in the western central  
1078 Atlantic Ocean. *Geophysical Journal International*, 72(1), 115-137.  
1079 <https://doi.org/10.1111/j.1365-246X.1983.tb02808.x>
- 1080
- 1081 Raitt, M. (1963). The crustal rocks. *The sea*, 3, 85-102.
- 1082
- 1083 Roland, E., Lizarralde, D., McGuire, J. J., & Collins, J. A. (2012). Seismic velocity  
1084 constraints on the material properties that control earthquake behavior at the Quebrada-  
1085 Discovery-Gofar transform faults, East Pacific Rise. *Journal of Geophysical Research:*  
1086 *Solid Earth*, 117(B11). <https://doi.org/10.1029/2012JB009422>

1087

1088 Sandwell, D. T. (1984). Thermomechanical evolution of oceanic fracture zones. *Journal of*  
1089 *Geophysical Research: Solid Earth*, 89(B13), 11401-11413.

1090 <https://doi.org/10.1029/JB089iB13p11401>

1091

1092 Sandwell, D. T., Müller, R. D., Smith, W. H., Garcia, E., & Francis, R. (2014). New global  
1093 marine gravity model from CryoSat-2 and Jason-1 reveals buried tectonic structure.

1094 *Science*, 346(6205), 65-67. <https://doi.org/10.1126/science.1258213>

1095

1096 Searle, R. C., Thomas, M. V., & Jones, E. J. W. (1994). Morphology and tectonics of the  
1097 Romanche Transform and its environs. *Marine Geophysical Researches*, 16(6), 427-

1098 453. <https://doi.org/10.1007/BF01270518>

1099

1100 Sykes, L. R. (1967). Mechanism of earthquakes and nature of faulting on the mid-oceanic  
1101 ridges. *Journal of Geophysical Research*, 72(8), 2131-2153.

1102 <https://doi.org/10.1029/JZ072i008p02131>

1103

1104 Taylor, M. A. J., & Singh, S. C. (2002). Composition and microstructure of magma bodies  
1105 from effective medium theory. *Geophysical Journal International*, 149(1), 15-21.

1106 <https://doi.org/10.1046/j.1365-246X.2002.01577.x>

1107

1108 Tolstoy, M., Harding, A. J., & Orcutt, J. A. (1993). Crustal thickness on the Mid-Atlantic  
1109 Ridge: Bull's-eye gravity anomalies and focused accretion. *Science*, 262(5134), 726-

1110 729. <https://doi.org/10.1126/science.262.5134.726>

1111

1112 Toomey, D. R., & Foulger, G. R. (1989). Tomographic inversion of local earthquake data  
1113 from the Hengill-Grensdalur central volcano complex, Iceland. *Journal of Geophysical*

- 1114            *Research: Solid Earth*, 94(B12), 17497-17510.  
1115            <https://doi.org/10.1029/JB094iB12p17497>
- 1116
- 1117            Van Avendonk, H. J., Davis, J. K., Harding, J. L., & Lawver, L. A. (2017). Decrease in  
1118            oceanic crustal thickness since the breakup of Pangaea. *Nature Geoscience*, 10(1), 58-  
1119            61. <https://doi.org/10.1038/ngeo2849>
- 1120
- 1121            Vaddineni, V. A., Singh, S.C., Grevemeyer, I., Audhkhasi, P., & Papenberg, C. (2021).  
1122            Evolution of the Crustal and upper Mantle seismic structure from 0-27 Ma in the  
1123            equatorial Atlantic Ocean at 2°43'S, *Journal of Geophysical Research: Solid Earth.*,  
1124            revised
- 1125
- 1126            Vine, F. J., & Moores, E. M. (1972). A model for the gross structure, petrology, and  
1127            magnetic properties of oceanic crust. *Studies in Earth and Space Sciences: A Memoir*  
1128            *in Honor of Harry Hammond Hess*, 195-205.
- 1129
- 1130            Wessel, P., Smith, W. H., Scharroo, R., Luis, J., & Wobbe, F. (2013). Generic mapping  
1131            tools: improved version released. *Eos, Transactions American Geophysical Union*,  
1132            94(45), 409-410. <https://doi.org/10.1002/2013EO450001>
- 1133
- 1134            White, R. S., Detrick, R. S., Sinha, M. C., & Cormier, M. H. (1984). Anomalous seismic  
1135            crustal structure of oceanic fracture zones. *Geophysical Journal International*, 79(3),  
1136            779-798. <https://doi.org/10.1111/j.1365-246X.1984.tb02868.x>
- 1137
- 1138            White, R. S., McKenzie, D., & O'Nions, R. K. (1992). Oceanic crustal thickness from  
1139            seismic measurements and rare earth element inversions. *Journal of Geophysical*  
1140            *Research: Solid Earth*, 97(B13), 19683-19715. <https://doi.org/10.1029/92JB01749>

1141

1142 Whitmarsh, R. B. (1978). Seismic refraction studies of the upper igneous crust in the North  
 1143 Atlantic and porosity estimates for layer 2. *Earth and Planetary Science Letters*, 37(3),  
 1144 451-464. [https://doi.org/10.1016/0012-821X\(78\)90061-4](https://doi.org/10.1016/0012-821X(78)90061-4)

1145

1146 Whitmarsh, R. B., & Calvert, A. J. (1986). Crustal structure of Atlantic fracture zones—I.  
 1147 The Charlie-Gibbs fracture zone. *Geophysical Journal International*, 85(1), 107-138.  
 1148 <https://doi.org/10.1111/j.1365-246X.1986.tb05174.x>

1149

1150 Wilson, J. T. (1965). A new class of faults and their bearing on continental drift. *Nature*,  
 1151 207(4995), 343-347.

1152

1153 Yilmaz, Ö. (2001). *Seismic data analysis: Processing, inversion, and interpretation of*  
 1154 *seismic data*. Society of exploration geophysicists.